

# Quantum Zeno Monte Carlo for computing observables

Mancheon Han,<sup>1,\*</sup> Hyowon Park,<sup>2,3,†</sup> and Sangkook Choi<sup>1,‡</sup>

<sup>1</sup>*School of Computational Sciences, Korea Institute for Advanced Study (KIAS), Seoul, 02455, Korea*

<sup>2</sup>*Materials Science Division, Argonne National Laboratory, Argonne, IL, 60439, USA*

<sup>3</sup>*Department of Physics, University of Illinois at Chicago, Chicago, IL, 60607, USA*

(Dated: May 10, 2024)

The recent development of logical quantum processors signifies a pivotal moment in the progression from the noisy intermediate-scale quantum (NISQ) era to the fault-tolerant quantum computing (FTQC) era. These advanced devices are poised to alter the approach to problems that challenge classical computation methods. By transforming such problems into Hamiltonian frameworks and exploiting quantum mechanical properties, these processors have the potential to address complex issues within a polynomial computational time. However, despite their advancements, these processors remain vulnerable to disruptive noise, highlighting the need for robust quantum algorithms designed to manage noise effectively. In response to this need, we introduce a new classical-quantum hybrid algorithm termed Quantum Zeno Monte Carlo (QZMC). QZMC is capable of handling device noises and Trotter errors while demonstrating polynomial computational cost. This algorithm combines the quantum Zeno effect with Monte Carlo integration techniques, facilitating multi-step transitions toward targeted eigenstates of the Hamiltonian problem. Notably, QZMC does not require overlap between the initial state and the target state, nor does it depend on variational parameters. It can compute static and dynamic properties of the targeted states, including ground state energy, excited state energies, and Green's functions. Compared to quantum phase estimation, QZMC offers a significantly reduced quantum circuit depth. These features make QZMC an important algorithm for navigating the current transitional phase in quantum computing and beyond.

## I. THE ONSET OF THE ERROR-CORRECTED QUANTUM COMPUTING ERA

The quantum computer [1–3] utilizes quantum algorithms to tackle computationally challenging problems, offering potential solutions to classically hard problems. A significant challenge lies in finding Hamiltonian eigenstates and their physical properties [4], crucial for material design and quantum machine learning implementation. By providing an initial state sufficiently close to the target eigenstate, this problem can be solved within polynomial quantum time [5, 6] with a fully fault-tolerant quantum computer (FTQC) [7, 8]. However, the preceding decades have been marked by the noisy intermediate-scale quantum (NISQ) era [9] rather than the FTQC era. Due to substantial device noise, quantum algorithms for NISQ systems prioritize noise resilience, leading to the dominance of ansatz-based algorithms [10, 11] without provable polynomial complexity.

The emergence of quantum devices with 48 logical qubits [12] marks the start of error-corrected quantum computing. These devices, along with their future advancements, have the potential to showcase quantum advantage, bridging the gap between NISQ and FTQC eras. Early error-corrected quantum computers are expected to handle longer quantum circuits than NISQ devices and execute quantum algorithms with polynomial complexity. However, algorithms designed for the FTQC era may not be suitable for early error-corrected quantum computers, as they still face device noise due to limited error corrections. As a result, developing new quantum al-

gorithms that costs polynomial quantum time and are resilient to noise shows promise for achieving quantum advantage in early error-corrected quantum computers.

We introduce the quantum Zeno Monte Carlo (QZMC) algorithm. This algorithm is robust against device noise as well as Trotter error. Furthermore, this algorithm enables the computation of static as well as dynamic physical properties for quantum systems within polynomial quantum time. Notably, QZMC does not necessitate overlap between the initial state and the target state, nor does it requires variational parameters. We validate its resilience to device noise by implementing it on IBM's NISQ devices for small systems. We also demonstrate its resilience to the Trotter error and the polynomial dependence of its computational cost by numerical demonstration on a noiseless quantum computer simulator. Then, we present theoretical computational cost of our method. Interestingly, the maximum quantum circuit depth required is notably shorter than that of the quantum phase estimation algorithm [13, 14].

## II. QUANTUM ZENO METHODS

The Quantum Zeno Monte Carlo algorithm draws inspiration from the quantum Zeno effect [15]. This is the phenomenon that repeated measurements slow down state transitions. We briefly outline this effect: A system varying with a continuous variable  $\lambda$  is represented by the state  $|\psi_\lambda\rangle$ . Increasing  $\lambda$  to  $\lambda + \Delta\lambda$  yields the state  $|\psi_{\lambda+\Delta\lambda}\rangle$ , which remains  $|\psi_\lambda\rangle$  with a probability of  $|\langle\psi_\lambda|\psi_{\lambda+\Delta\lambda}\rangle|^2$ . Because its maximum is at  $\Delta\lambda = 0$ , this probability becomes  $1 - \mathcal{O}((\Delta\lambda)^2)$  for sufficiently small  $\Delta\lambda$ . By dividing  $\Delta\lambda$  into  $N$  slices and measuring at each interval of  $\Delta\lambda/N$ , the probability of measuring  $|\psi_\lambda\rangle$  is  $1 - \mathcal{O}((\Delta\lambda)^2/N)$ . Increasing the measurement fre-

\* mchan@kias.re.kr

† hyowon@uic.edu

‡ sangkookchoi@kias.re.kr

quency  $N$  ensures the system remains in its initial state  $|\psi_\lambda\rangle$ .

While the original article [15] focused on state freezing through continuous measurements, the principle can also be applied to obtain an energy eigenstate by varying the Hamiltonian for each measurement [16–20]. Let's denote our target Hamiltonian as  $H$ , with its eigenstate as  $|\Phi\rangle$ . Suppose we have an easily preparable eigenstate  $|\Phi_0\rangle$  of  $H_0$  and the state is adiabatically connected to  $|\Phi\rangle$ . Due to the Van Vleck catastrophe [21, 22],  $|\Phi_0\rangle$  has very small overlap with  $|\Phi\rangle$  in general, potentially requiring a large number of measurements to obtain  $|\Phi\rangle$  directly from  $|\Phi_0\rangle$ . Instead, we consider measuring  $H_\alpha = (1 - \lambda_\alpha)H_0 + \lambda_\alpha H$  consecutively for  $\lambda_\alpha = 1/N_\alpha, 2/N_\alpha, \dots, 1$ . Utilizing the quantum Zeno principle, we can obtain  $|\Phi\rangle$  with very high probability as we increase the number of consecutive measurements  $N_\alpha$ .

### III. QUANTUM ZENO MONTE CARLO

The quantum Zeno principle can be implemented using projections, which is equivalent to measurements. Let's consider  $H_\alpha = (1 - \lambda_\alpha)H_0 + \lambda_\alpha H$  where  $\lambda_\alpha = 1/N_\alpha, 2/N_\alpha, \dots, 1$ , and  $|\Phi_0\rangle$  is the eigenstate of  $H_0$  that can be readily prepared. For the eigenstate  $|\Phi_\alpha\rangle$  of  $H_\alpha$ , the operator that projects onto  $|\Phi_\alpha\rangle$  is represented as  $|\Phi_\alpha\rangle\langle\Phi_\alpha|$ . Then, the consecutive projections  $\mathcal{P}_\alpha$  applied to  $|\Phi_0\rangle$  is

$$|\Psi_\alpha\rangle = \mathcal{P}_\alpha |\Phi_0\rangle, \quad \mathcal{P}_\alpha = |\Phi_\alpha\rangle\langle\Phi_\alpha| \dots |\Phi_1\rangle\langle\Phi_1|, \quad (1)$$

which is equal to  $|\Phi_\alpha\rangle$  apart from the normalization. The quantum Zeno principle ensures that  $\langle\Psi_\alpha|\Psi_\alpha\rangle = \langle\Phi_0|\mathcal{P}_\alpha^\dagger\mathcal{P}_\alpha|\Phi_0\rangle$  approaches 1 as  $N_\alpha \rightarrow \infty$ . For the implementation of  $\mathcal{P}_\alpha$ , we use the approximate projection operator defined as

$$P_H^\beta(E) = \sum_j |j\rangle\langle j| e^{-\beta^2(\mathcal{E}_j - E)^2/2} = e^{-\beta^2(H - E)^2/2}, \quad (2)$$

while  $\mathcal{E}_j$  and  $|j\rangle$  are energy eigenvalues and eigenstates for a Hamiltonian  $H$ . As  $\beta$  increases, Eq. (2) becomes the projection onto the subspace with the energy  $E$ . Its implementation on the quantum computer can be achieved by using the Fourier expansion [23–26]

$$P_H^\beta(E) = \frac{1}{\sqrt{2\pi\beta^2}} \int_{-\infty}^{\infty} e^{-\frac{t^2}{2\beta^2}} e^{-i(H - E)t} dt. \quad (3)$$

The integrand in Eq. (3) represents the time evolution which can be implemented within a polynomial quantum time [27, 28]. Then, the consecutive projection  $\mathcal{P}_\alpha$  can be approximated by

$$\mathcal{P}_\alpha^\beta = P_{H_\alpha}^\beta(E_\alpha) \dots P_{H_1}^\beta(E_1), \quad (4)$$

while  $E_\alpha$  is the energy eigenvalue of  $H_\alpha$  corresponds to  $|\Phi_\alpha\rangle$ . By substituting  $\mathcal{P}_\alpha$  by  $\mathcal{P}_\alpha^\beta$ , consecutive projection transforms into a multidimensional integral of consecutive time evolution, which can be computed using the Monte Carlo method [29]. Like recently proposed algorithms [23, 24], our

objective is to compute the expectation values  $\langle O \rangle$  of observables rather than the state itself. By using  $|\Psi_\alpha\rangle$ ,  $\langle O \rangle_\alpha = \langle\Phi_\alpha|O|\Phi_\alpha\rangle$  can be determined as

$$\langle O \rangle_\alpha = \frac{\langle\Psi_\alpha|O|\Psi_\alpha\rangle}{\langle\Psi_\alpha|\Psi_\alpha\rangle}, \quad (5)$$

where  $\langle\Psi_\alpha|A|\Psi_\alpha\rangle$  for an arbitrary operator  $A$  is computed by the summation of consecutive time evolutions,

$$\langle\Psi_\alpha|A|\Psi_\alpha\rangle = \frac{1}{N_\nu} \sum_\nu \langle\Phi_0|e^{-iK_1 t_{\nu,2\alpha}} \dots e^{-iK_\alpha t_{\nu,\alpha+1}} A e^{-iK_\alpha t_{\nu,\alpha}} \dots e^{-iK_1 t_{\nu,1}} |\Phi_0\rangle. \quad (6)$$

Here,  $K_{\alpha'} = H_{\alpha'} - E_{\alpha'}$  for  $\alpha' = 1, \dots, \alpha$  and we use  $N_\nu$  samples of  $\mathbf{t}_\nu = [t_{\nu,1} \ t_{\nu,2} \ \dots \ t_{\nu,2\alpha}]^T$ , where each  $t_{\nu,k}$  is drawn from the gaussian distribution with a standard deviation of  $\beta$ . Consequently, various static and dynamic properties of Hamiltonian eigenstates can be computed using the aforementioned quantum Zeno Monte Carlo (QZMC) method. Figure 1 provides a summary of QZMC.

The QZMC computation relies on prior knowledge of energy eigenvalues  $E_\alpha$ . Therefore, a practical method for their computation is necessary. Here, we propose the predictor-corrector QZMC method for determining energy eigenvalues. Suppose we know  $E_0, E_1, \dots, E_{\alpha-1}$  and aim to compute  $E_\alpha$ . Similar to the predictor-corrector method used in solving differential equations [30], we begin with a rough estimate of  $E_\alpha$ , termed the predictor. Our predictor for  $E_\alpha$  is the first-order perturbation approximation [31], given by  $E_\alpha = E_{\alpha-1} + \langle\Phi_{\alpha-1}|h_{\alpha-1}|\Phi_{\alpha-1}\rangle$ , where  $h_{\alpha-1} = H_\alpha - H_{\alpha-1}$ . Subsequently, using the predictor  $E_\alpha$ , we compute a more accurate estimate of  $E_\alpha$ , termed the corrector. We determine the corrector based on the properties of the consecutive projection,

$$E_\alpha = E_{\alpha-1} + \frac{\langle\Psi_\alpha|\Phi_\alpha\rangle\langle\Phi_\alpha|h_{\alpha-1}|\Psi_{\alpha-1}\rangle}{\langle\Psi_\alpha|\Psi_\alpha\rangle}. \quad (7)$$

This equation directly computes the energy difference  $E_\alpha - E_{\alpha-1}$  using QZMC. Compared to estimating the entire energy, this approach enhances robustness against noise by confining noise influences to the energy difference ( $E_\alpha - E_{\alpha-1}$ ) alone. Based on this insight, we employed Eq. (7), which can be computed as in Eq. (6) by substituting  $|\Phi_\alpha\rangle\langle\Phi_\alpha|$  by  $P_H^\beta(E_\alpha)$ . More details of QZMC as well as its extension to compute Green's function are described in the Appendix. A.

Our method starts with the assumption that we have  $H_0$ , which can be easily solved with a classical computer, and that the eigenstate is readily preparable as a quantum circuit. However, arbitrary unitary synthesis can incur exponential quantum time costs [32], making the preparation of the eigenstate  $|\Phi_0\rangle$  challenging even when  $H_0$  can be exactly solved with a classical computer. In such cases, we prepare an easily accessible state  $|\tilde{\Phi}_0\rangle$  which has a non-trivial overlap with  $|\Phi_0\rangle$  (e.g.  $|\langle\Phi_0|\tilde{\Phi}_0\rangle|^2 > 0.5$ ). Then, we project  $|\tilde{\Phi}_0\rangle$  onto  $|\Phi_0\rangle$  by using Eq. (2) and perform QZMC in an equivalent way. Therefore,

$$|\Psi_\alpha\rangle = \mathcal{P}_\alpha |\Phi_0\rangle \langle\Phi_0|\tilde{\Phi}_0\rangle, \quad (8)$$

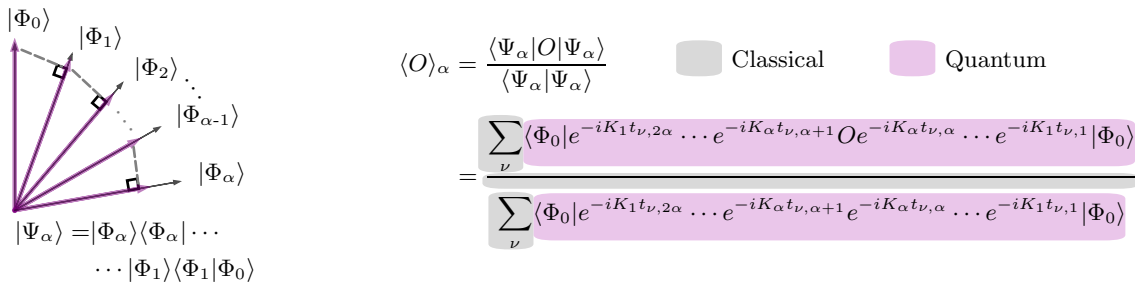


Figure 1. Overview of the Quantum Zeno Monte Carlo. The construction of the unnormalized eigenstate  $|\Psi_\alpha\rangle$  of  $H_\alpha$  from the eigenstate  $|\Phi_0\rangle$  of  $H_0$  is depicted (left). Each  $|\Phi_k\rangle$  represents the normalized eigenstate of  $H_k$ . In the right, we present a summary of our Quantum Zeno Monte Carlo for computing the expectation value of an observable ( $O$ ). First, classical computer generates a time vector  $\mathbf{t}_\nu = [t_{\nu,1} \ t_{\nu,2} \ \dots \ t_{\nu,2\alpha}]^T$ , where  $t_{\nu,k}$  follows Gaussian distribution. Next, quantum computer measure the expectation value with the given time vector. Finally, the sum over  $N_\nu$  Monte Carlo sampling as well as the division is conducted by using classical computer. Here,  $K_{\alpha'}$  represents  $H_{\alpha'} - E_{\alpha'}$ .

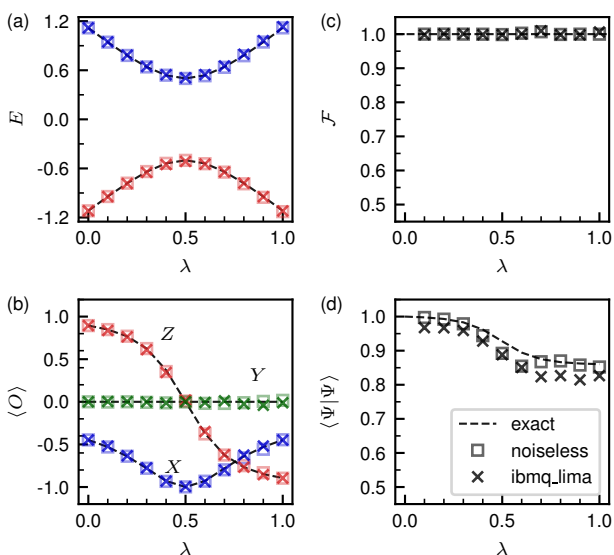


Figure 2. A one-qubit system. The energy eigenvalues of the ground (red) and the excited state (blue) are plotted in (a). In (b), we plotted  $\langle X \rangle$  (blue),  $\langle Y \rangle$  (green), and  $\langle Z \rangle$  (red) calculated for the ground states. (c) and (d) display the fidelity  $\mathcal{F}$  and  $\langle \Psi | \Psi \rangle$  for the ground state. In (a)-(d), dotted lines represent the exact result, boxes represent QZMC results with a noiseless simulator, and crosses represent results with *ibmq\_lima*. In this figure, we used  $\beta = 5$  and  $N_\nu = 400$ .

instead of Eq. (1). As  $|\Phi_0\rangle$  is known and can be processed with a classical computer, finding  $|\tilde{\Phi}_0\rangle$  can be efficiently accomplished using classical computing resources.

#### IV. APPLICATIONS OF QZMC

Here, we verify our method by applying it to solve various quantum many body systems. First, we used our method to compute physical properties of small systems with NISQ devices. The first system we consider (Figure 2) is the one-

qubit system with the Hamiltonian.  $H(\lambda) = X/2 + (2\lambda - 1)Z$ . Next, we simulate the  $H_2$  molecule (Figure 3 (a)) in the STO-3G basis [33], a typical testbed for quantum algorithms [34, 35]. By constraining the electron number to be 2 and the total spin to be 0 [36, 37], the system can be represented by a 2-qubit Hamiltonian. We calculate the energy spectrum of  $H_2$  as a function of interatomic distance ( $R$ ). Lastly, we consider the 2-site Hubbard model [38]. The Hubbard dimer (Figure 3 (b)-(f)) at its half filling and singlet spin configuration can also be mapped to a two-qubit Hamiltonian. Energy eigenvalues of the Hubbard dimer are computed by increasing onsite Coulomb interaction ( $U$ ). For these calculations, we create a discrete path with  $N_\alpha = 10$ , and apply the predictor-corrector QZMC for  $H_\alpha = H(\lambda_\alpha)$  (For more details of the NISQ simulations, see Appendix B).

The one-qubit system results are displayed in Fig. 2. Fig. 2 (a) shows the ground and the excited state energy eigenvalues, while Fig. 2 (b) shows ground state expectation value of  $X$ ,  $Y$  and  $Z$  operators. Despite device noises in *ibmq\_lima*, measured observables match well with exact values (dashed lines). Moreover, computed ground state fidelity  $\mathcal{F}_\alpha = |\langle \Phi_\alpha | \Psi_\alpha \rangle|^2 / \langle \Psi_\alpha | \Psi_\alpha \rangle$  (Fig. 2 (c)) is almost 1, which demonstrates accurate projection to the desired state by QZMC.

Figure 3 presents computational results for two-qubit systems:  $H_2$  and the Hubbard dimer. We determined the energy eigenvalues of  $H_2$  within an error of 0.02 Ha using *ibmq\_lagos*. Energy eigenvalues for the Hubbard dimer are calculated within an error of 0.06  $t$  on *ibmq\_perth*, where  $t$  is electron hopping between two hubbard atoms. And we compute the electronic spectral function  $A(\omega)$  [39] of the Hubbard dimer with the NISQ device. Figures 3 (e)-(f) displays  $A(\omega)$  at  $k = 0$  and  $k = \pi$ , showing good agreements between exact values and measured values.

Next, we demonstrate our method for a large system by applying QZMC on the Hubbard model at the half-filling in various sizes with noiseless qsim-cirq [40] quantum computer simulator. As  $H_0$ , we choose dimer array, featuring easily implementable non-degenerate ground state. We gradually increased the inter-dimer hopping  $t_{\text{inter}}$  from 0 to the desired

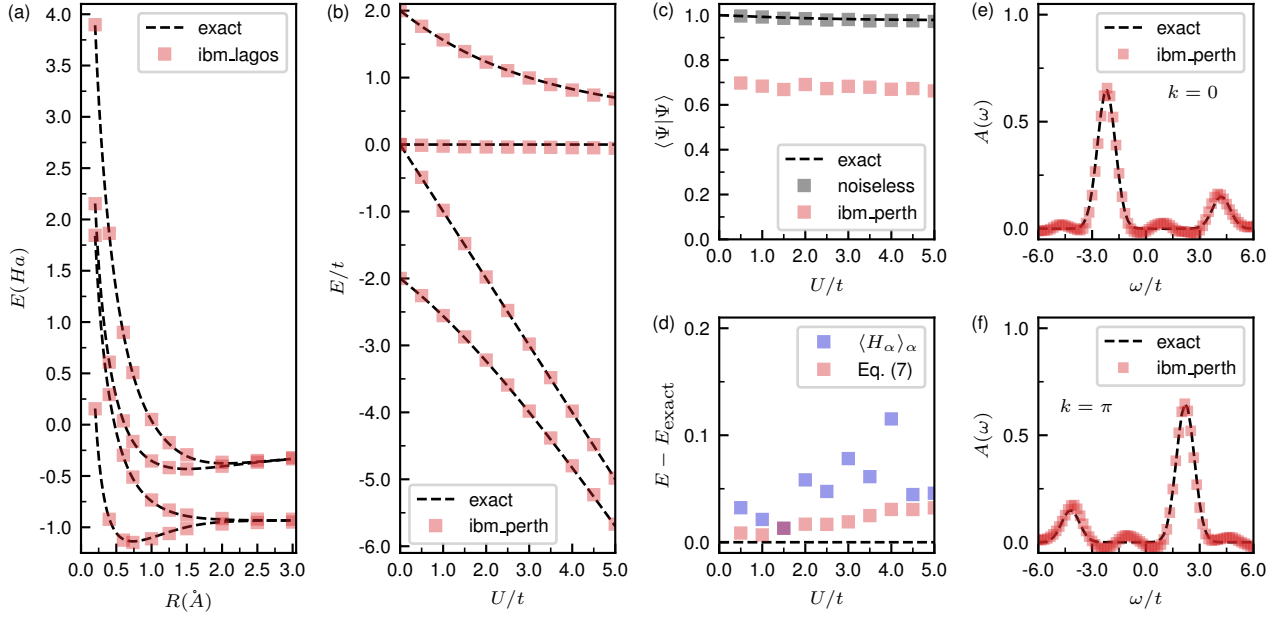


Figure 3.  $H_2$  and the Hubbard dimer. (a) plots energy eigenvalues of  $H_2$  in a STO-3G basis as a function of the bond length. Here, we used  $\beta = 5$  and NISQ device calculation is conducted with *ibm\_lagos*. In (b)-(f), we considered the Hubbard dimer. (b) shows energy eigenvalues as a function of the Coulomb interaction  $U$ . In (c), we compared  $\langle \Psi | \Psi \rangle$  of the ground state calculated with the NISQ device with exact values and noiseless QZMC results. (d) compares two energy estimator  $\langle H_\alpha \rangle_\alpha = \langle \Phi_\alpha | H_\alpha | \Phi_\alpha \rangle$  and Eq. (7). The spectral functions for two different crystal momentum (e)  $k = 0$  and (f)  $k = \pi$  are plotted. For the Hubbard dimer, we used  $\beta = 0.5$  and *ibm\_perth* is used. In this figure, we used  $N_\nu = 100$  Monte Carlo samples for each  $\alpha$  and the spectral function is calculated with 300 Monte Carlo samples.

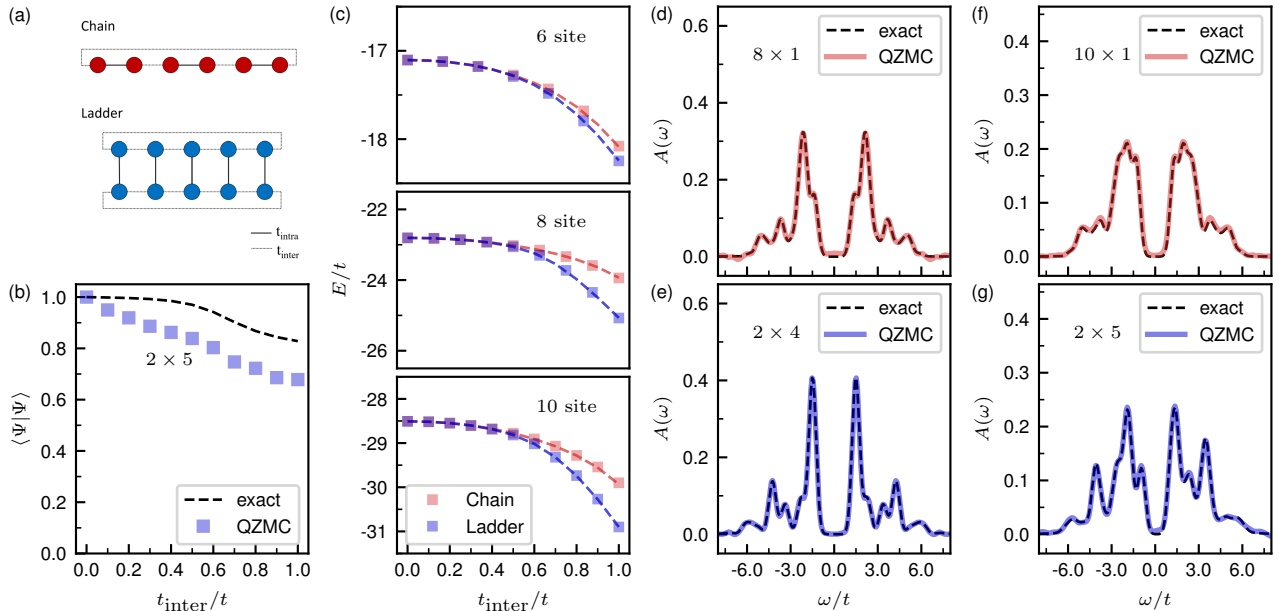


Figure 4. The Hubbard model in various sizes. (a) shows two geometries we considered. Here, colored circles denote sites, solid lines indicate intra-dimer hopping  $t_{\text{intra}}$ , and dotted lines represent inter-dimer hopping  $t_{\text{inter}}$ . (b) displays  $\langle \Psi | \Psi \rangle$  for the  $2 \times 5$  Hubbard model as a function of  $t_{\text{inter}}$ , while (c) presents ground state energy eigenvalues computed from QZMC. In each subplot of (c), red squares denote energies for  $6 \times 1$ ,  $8 \times 1$ , and  $10 \times 1$  models with QZMC, with red dotted lines indicating corresponding exact values. Blue squares and lines represent the same values for  $2 \times 3$ ,  $2 \times 4$ , and  $2 \times 5$  cases. (d)-(g) depict the local spectral function for the Hubbard models.

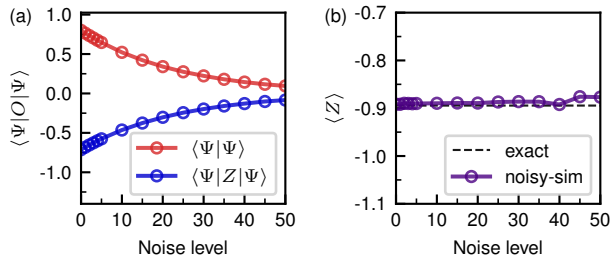


Figure 5. Noise resilience of the observable.  $\langle \Psi|\Psi \rangle$ ,  $\langle \Psi|Z|\Psi \rangle$ , and  $\langle Z \rangle$  of the one-qubit system considered in the Fig. 2 are drawn as a function of the noise level. The calculations are conducted with the qiskit noisy simulator using the noise model of *ibmq lima*. In this figure, we used  $N_\alpha = 10$ ,  $\beta = 5$  and  $N_\nu = 400$ .

value  $t$  as  $\alpha$  increased. We explored two geometries, chains and ladders, with periodic boundary conditions, as illustrated in Figure 4 (a). For each geometry, we computed systems with 6, 8, and 10 sites when  $U/t = 5$ . For QZMC, we used  $\beta = 3$ , with  $N_\alpha$  equal to the number of sites and  $N_\nu$  increases as  $h_\alpha$  increases. For the time evolution, we used the first order Trotterization [27, 41, 42], adjusting the Trotter steps as system changes. (See Appendix. C for the quantum circuit for the ground state of the dimer and details on the choice of  $N_\nu$  and the number of Trotter steps).

Fig. 4 (c) shows that QZMC accurately reproduces the exact ground state energy across various configurations, from 6 to 10 sites, in both chain and ladder arrangements. And our method also accurately computes local spectral function for Hubbard models as shown in in Fig. 4 (d)-(g), which reproduces the exact positions and widths of every peak in the spectral functions.

## V. RESILIENCE TO DEVICE NOISE AND TROTTER ERROR

Interestingly, our calculational results for observables accurately reproduce exact values even with the device noises (Fig. 2 and Fig. 3) and the Trotter errors (Fig. 4). Actually, the effect of these noises induces significant deviations of calculated  $\langle \Psi|\Psi \rangle$  (Fig. 2 (d), Fig. 3 (c), and Fig. 4 (b)) from exact values. However, the observable expectation values, which is computed by using the ratio of  $\langle \Psi|O|\Psi \rangle$  and  $\langle \Psi|\Psi \rangle$  (Eq. (5)) is robust against device noises and Trotter errors. To understand this, we tested the dependence of the calculated observables on the device noise magnitude using the qiskit [43] aer simulator. We considered  $\langle \Psi|\Psi \rangle$ ,  $\langle \Psi|Z|\Psi \rangle$ , and  $\langle Z \rangle$  of the ground state of the one-qubit system. Figure. 5 shows calculational results. As the noise level increases,  $\langle \Psi|\Psi \rangle$  decreases and the absolute value of  $\langle \Psi|Z|\Psi \rangle$  also decreases (Fig. 2 (a)). Surprisingly, these noise-induced errors cancel each other through the ratio of  $\langle \Psi|\Psi \rangle$  and  $\langle \Psi|Z|\Psi \rangle$ , so that  $\langle Z \rangle = \langle \Psi|Z|\Psi \rangle / \langle \Psi|\Psi \rangle$  (Fig 2 (b)) remains robust against noise. Since quantum circuits for computing the numerator and denominator are nearly identical, division cancels

out common noise effects, making the expectation value resilient to noise. The same argument applies to Trotterization; thus, the method is resilient to Trotter error too. Because we use same Trotterization rule for both the numerator and the denominator, common Trotterization errors are canceled out by division. This cancellation results in precise reproduction of energies and spectral functions in Fig. 4 (c)-(g), while the Trotterization error makes  $\langle \Psi|\Psi \rangle$  (Fig. 4 (b)) deviates largely from the exact values.

To understand how noise cancellation occurs, it is essential to be clear about the circumstances of the calculation. In our method, we measure consecutive time evolution using a single ancilla qubit (See Appendix. A 6 for quantum circuits). With this in mind, let's examine the following simple example. Consider a qubit with the density matrix  $\rho$ . Then, exact outcome of a  $Z$  measurement on this qubit is given by  $\text{Tr}(\rho Z)$ . The effect of noise the qubit can be described as a transformation of the density matrix  $\rho$  to  $\mathcal{E}(\rho)$  [3]. With this noise, the outcome of the  $Z$  measurement becomes  $\text{Tr}(\mathcal{E}(\rho)Z)$ . Consider the depolarizing channel as a specific type of noise, which alters the state  $\rho$  to  $\mathcal{E}(\rho) = pI/2 + (1-p)\rho$ . Here,  $p$  represents the probability of depolarization. With this model,  $\text{Tr}(\mathcal{E}(\rho)Z)$  becomes  $(1-p)\text{Tr}(\rho Z)$ . Now, imagine another qubit with the density matrix  $\rho'$  subjected to the same noise channel. The  $Z$  measurement of this qubit yields  $(1-p)\text{Tr}(\rho'Z)$ . Then, the ratio of the measurement outcomes of two qubits with noise channel is

$$\frac{\text{Tr}(\mathcal{E}(\rho')Z)}{\text{Tr}(\mathcal{E}(\rho)Z)} = \frac{(1-p)\text{Tr}(\rho'Z)}{(1-p)\text{Tr}(\rho Z)} = \frac{\text{Tr}(\rho'Z)}{\text{Tr}(\rho Z)}, \quad (9)$$

which is same with the exact value. This demonstrates that the effect noise can be effectively canceled out by the division. Though we only showed the case with the depolarizing channel, same cancellation occurs for bit and phase flip channels.

In addition to the noise cancellation effect demonstrated in Fig. 5, the use of estimator Eq. (7), which only computes the energy differences, makes energy estimation more robust against noise by limiting the influence of the noise for the energy difference  $E_\alpha - E_{\alpha-1}$  only. Fig. 3 (d) shows this. In this figure, we can see that noise induced deviations observed in  $\langle H_\alpha \rangle_\alpha = \langle \Phi_\alpha | H_\alpha | \Phi_\alpha \rangle$  is absent in the calculation with the formula Eq. (7).

## VI. COMPUTATIONAL COST

In this section, we summarize the theoretical computational cost of our method, which is explained in the Appendix. A 4 more detail. To simplify the discussion, we consider linear interpolation between  $H_0$  and  $H$ , represented by  $H_\alpha = H_0 + \lambda_\alpha H'$ , where  $H' = H - H_0$  and  $\lambda_\alpha = 1/N_\alpha, 2/N_\alpha, \dots, 1$ . Then, we focus solely on the ground state energy estimation cost. Let's first examine  $N_\nu$ , the number of Monte Carlo samples. Our energy difference estimation in Eq. (7) involves a Monte Carlo summation of  $\langle \Phi_0 | e^{-iK_1 t_\nu, 2\alpha} \dots e^{-iK_\alpha t_\nu, \alpha+1} e^{-iK_\alpha t_\nu, \alpha} H' \dots e^{-iK_1 t_\nu, 1} | \Phi_0 \rangle$ . Since time evolution is unitary, each term in the summation is

bounded by  $\|H'\|$ , resulting in a Monte Carlo error  $\epsilon$  bounded by  $\|H'\|/\sqrt{N_\nu}$ . Hence, the appropriate number of Monte Carlo samples  $N_\nu$  is proportional to  $\|H'\|^2/\epsilon^2$ . In most cases,  $H'$  can be represented as a sum of a polynomial number of Pauli strings [44], which gives  $\mathcal{O}(\text{poly}(n))$  upperbound of  $\|H'\|$ . Here  $n$  is the number of qubits. Therefore, we can state that  $N_\nu$  is  $\mathcal{O}(\text{poly}(n))/\epsilon^2$ . Next, let's consider  $N_\alpha$  which determines the total number of consecutive time evolutions. According to the perturbation theory [31],  $\langle \Psi_\alpha | \Psi_\alpha \rangle \geq 1 - \|H'\|/(\Delta_g N_\alpha)$ . Therefore, for a finite norm, we must have  $N_\alpha \propto \|H'\|/\Delta_g$ . Lastly, let's determine  $\beta$ , the width of each projection. For each projection, perturbative analysis shows that energy estimation error comes from finite  $\beta$  is proportional to  $\exp(-\beta^2 \Delta_g^2/2) \|H'\|^2/\Delta_g$ . To ensure this quantity is smaller than error  $\epsilon$ ,  $\beta$  should be proportional to  $\Delta_g^{-1} \sqrt{\log(2\|H'\|^2/(\epsilon \Delta_g))}$ . Then, the required time evolution length, which is proportional to  $N_\alpha \beta$ , is  $\mathcal{O}(\Delta_g^{-2} \text{poly}(n) \sqrt{\log(\mathcal{O}(\Delta_g^{-1} \epsilon^{-1} \text{poly}(n))))}$ . Because each of time evolution falls within the complexity class BQP (bounded-error quantum polynomial time) [45], we can conclude that QZMC provides energy eigenvalues and various physical properties within a polynomial quantum time, as long as the energy gap  $\Delta_g$  does not decrease superpolynomially. We summarized and compared the computational cost for the ground state energy estimation of our method with other methods at Table. I.

Finally, we compared the maximum time evolution length (which is proportional to the circuit depth) of QZMC for estimating the ground state energy of Hubbard chains with other methods [20, 46] in Fig. 6. In contrast to references [20, 46], which assumed exact time evolutions, we used the Trotterized time evolution with same trotter step rule used in Fig. 4. To make similar initial condition with references, we prepared the initial state  $|\Phi_0\rangle$  with  $|\langle \Phi | \Phi_0 \rangle|^2 = 0.4$  and applied QZMC with Eq. (8). We fixed  $N_\alpha = 4$  and increased  $\beta$  to decrease energy estimation error  $\epsilon$ . For the maximum time evolution length  $T$  of QZMC, we used the 90th percentile of distribution of time evolution length  $|t_{\nu,1}| + \dots + |t_{\nu,2N_\alpha}|$  (i.e. 90% of time evolution length is smaller than  $T$ ). Figure 6 (a) compares QZMC with Ref. [47], which shows that significant circuit depth reduction of our method compared to the reference. Comparison of our method with QCELS [46] and QPE are shown in Fig. 6 (b)-(c). As depicted in the figure, our method requires a much smaller circuit depth than QPE, and it is similar to Ref.[46].

## VII. CONCLUSION

In this work, we introduced the quantum Zeno Monte Carlo (QZMC) for the emerging stepping stone era of quantum computing [12]. This method computes static and dynamical observables of quantum systems within a polynomial quantum time, without the need for variational parameters. Leveraging the Quantum Zeno effect, we progressively approach the unknown eigenstate from the readily solvable Hamiltonian's eigenstate. This aspect distinguishes our method from

other methods for phase estimations, which necessitate an initial state with significant overlap with the desired eigenstate [5, 6, 24, 25, 46, 47, 49]. Preparing a state with substantial overlap with an eigenstate of an easily solvable Hamiltonian is much simpler than preparing an initial state with non-trivial overlap with the unknown eigenstate, making our algorithm highly practical compared to other methods. Next characteristic of the algorithm is its computation of eigenstate properties by dividing the properties of the unnormalized eigenstate by its norm squared (Eq. (5)). We demonstrated that this approach effectively cancels out noise effects in the denominator and the numerator, rendering the method resilient to device noise as well as Trotter error. This resilience arises from the similar noise levels experienced by both the denominator and the numerator of observable expectation value, leading us to conclude that our approach is well-suited for homogeneous parallel quantum computing.

## VIII. ACKNOWLEDGMENT

We thank Hyukjoon Kwon, Joonsuk Huh, and Lin Lin for their insightful comments and discussions. This research was supported by Quantum Simulator Development Project for Materials Innovation through the National Research Foundation of Korea (NRF) funded by the Korean government (Ministry of Science and ICT(MSIT))(No. NRF-2023M3K5A1094813). For one and two qubit simulations, we acknowledge the use of IBM Quantum services for this work and to advanced services provided by the IBM Quantum Researchers Program. The views expressed are those of the authors, and do not reflect the official policy or position of IBM or the IBM Quantum team. For larger system calculation, we used resources of the Center for Advanced Computation at Korea Institute for Advanced Study and the National Energy Research Scientific Computing Center (NERSC), a U.S. Department of Energy Office of Science User Facility operated under Contract No. DE-AC02-05CH11231. SC was supported by a KIAS Individual Grant (CG090601) at Korea Institute for Advanced Study. M.H. is supported by a KIAS Individual Grant (No. CG091301) at Korea Institute for Advanced Study.

## Appendix A: Equations for Quantum Zeno Monte Carlo

This section discuss details of the quantum Zeno Monte Carlo.

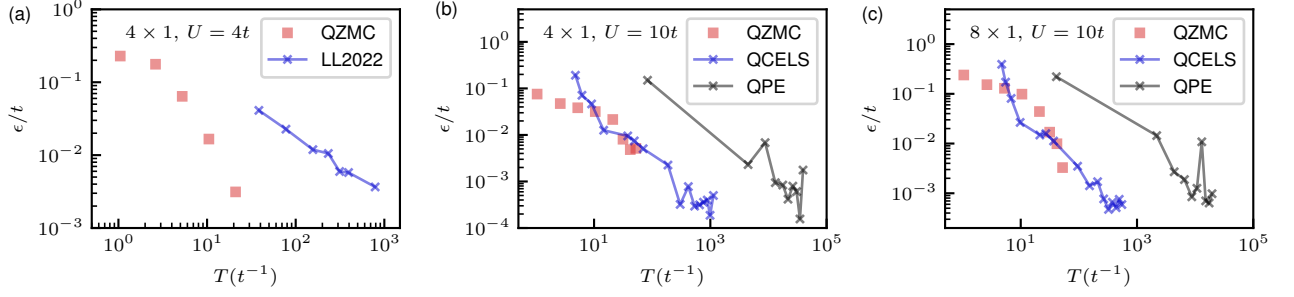


Figure 6. Comparison with other methods. (a)-(c) plots ground state energy error  $\epsilon$  as a function of the maximum time evolution length  $T$ . (a) considers  $4 \times 1$  Hubbard model with  $U = 4t$ , (b) computes  $4 \times 1$  Hubbard model with  $U = 10t$ , and  $8 \times 1$  Hubbard model with  $U = 10t$  is considered in (c). In (a), blue points represents the data from Ref. [47]. And QCELS and QPE data in (b)-(c) are imported from Ref. [46] with unit conversion.

Table I. Computational cost of QZMC and other quantum algorithms

	Maximum time evolution length	Repetitions
QZMC	$\mathcal{O}(\Delta_g^{-2} \text{poly}(n))(\log(\mathcal{O}(\Delta_g^{-1} \epsilon^{-1} \text{poly}(n))))^{1/2}$	$\mathcal{O}(\epsilon^{-2} \text{poly}(n))$
QPE [13, 14]	$\tilde{\mathcal{O}}(\epsilon^{-1} p_0^{-1})$	$\tilde{\mathcal{O}}(p_0^{-1} \text{polylog}(\epsilon^{-1}))$
QEEA [48]	$\tilde{\mathcal{O}}(\epsilon^{-1} \text{polylog}(p_0^{-1}))$	$\tilde{\mathcal{O}}(\epsilon^{-3} p_0^{-2})$
Ref. [47]	$\tilde{\mathcal{O}}(\epsilon^{-1} \text{polylog}(p_0^{-1}))$	$\tilde{\mathcal{O}}(p_0^{-2} \text{polylog}(\epsilon^{-1}))$
Ref. [25]	$\mathcal{O}(\Delta_g^{-1} \text{polylog}(\epsilon^{-1} p_0^{-1} \Delta_g))$	$\mathcal{O}(p_0^{-2} \epsilon^{-2} \Delta_g^2)$

<sup>a</sup> This table summarize the cost of QZMC to compute energy eigenvalues and compares it with several other quantum algorithms that computes energy eigenvalues within a single ancilla qubit. Complexity analysis of QPE and QEEA imported from Ref. [47]. Here,  $p_0$  the probability of getting exact eigenstate from the initial states,  $\epsilon$  is a desired precision in the energy, and  $n$  is the number of qubits. Optimized algorithms for highly overlapped initial states [46, 49] shows similar dependence with algorithm of Ref. [47], only constant factor is different.

## 1. Static observables

First, we show the derivation of Eq. (6). By substituting  $\mathcal{P}_\alpha$  by  $\mathcal{P}_\alpha^\beta$ ,  $\langle \Psi_\alpha | A | \Psi_\alpha \rangle = \langle \Phi_0 | \mathcal{P}_\alpha^\dagger A \mathcal{P}_\alpha | \Phi_0 \rangle$  becomes

$$\langle \Psi_\alpha | A | \Psi_\alpha \rangle = \frac{1}{(2\pi\beta^2)^\alpha} \int e^{-\sum_{a=1}^{2\alpha} \frac{t_a^2}{2\beta^2} + i\phi_\alpha(t)} \langle \Phi_0 | e^{-iH_1 t_{2\alpha}} \dots e^{-iH_\alpha t_{\alpha+1}} A e^{-iH_\alpha t_\alpha} \dots e^{-iH_1 t_1} | \Phi_0 \rangle dt, \\ \phi_\alpha(t) = \sum_{\alpha'=1}^{\alpha} E_{\alpha'}(t_{\alpha'} + t_{2\alpha+1-\alpha'}) \quad (\text{A1})$$

This multi-dimensional integration can be efficiently calculated by using the Monte Carlo method [29] with  $\{t_a \sim \mathcal{N}(0, \beta)\}$ . This yields Eq. (6). The measurement of  $\langle \Phi_0 | e^{-iH_1 t_{2\alpha}} \dots e^{-iH_\alpha t_{\alpha+1}} A e^{-iH_\alpha t_\alpha} \dots e^{-iH_1 t_1} | \Phi_0 \rangle$  on the quantum computer can be achieved through the Pauli string [44] expansion of operator  $A$ . Then, the expectation value of the observable  $O$  is obtained through Eq. (5) by inserting  $A = O$  to the numerator and  $A = \mathbb{I}$  for the denominator.

## 2. Green's function

Next, we derive the Quantum Zeno Monte Carlo method for computing the electronic Green's function. The computation of other Green's function, such as the spin-spin

correlation function, follows a similar approach. The retarded electronic Green's function is defined as  $G_{jk}^R(t) = -i\theta(t) \langle \Phi | \{c_j(t), c_k^\dagger(0)\} | \Phi \rangle$ , where  $\{, \}$  represents the anti-commutator and  $c_j$  ( $c_j^\dagger$ ) is the annihilation (creation) operator for the  $j$ -th orbital. This function can be expressed compactly using the spectral function  $A_{jk}(\omega)$ ,

$$G_{jk}^R(\omega + i0^+) = \int_{-\infty}^{\infty} \frac{A_{jk}(\omega')}{\omega + i0^+ - \omega'} d\omega'. \quad (\text{A2})$$

The spectral function  $A_{jk}(\omega)$  is expanded in [39]

$$A_{jk}(\omega) = A_{jk,1}(\omega) + A_{jk,2}(\omega), \\ A_{jk,1}(\omega) = \sum_m \langle \Phi | c_j | m \rangle \langle m | c_k^\dagger | \Phi \rangle \delta(\mathcal{E}_m - \mathcal{E}_\Phi - \omega), \\ A_{jk,2}(\omega) = \sum_m \langle \Phi | c_k^\dagger | m \rangle \langle m | c_j | \Phi \rangle \delta(\mathcal{E}_m - \mathcal{E}_\Phi + \omega). \quad (\text{A3})$$

While  $|m\rangle$  and  $\mathcal{E}_m$  are the energy eigenstate and corresponding energy eigenvalue. We focus on computing  $A_{jk,1}(\omega)$ , as  $A_{jk,2}(\omega)$  can be computed similarly. The dirac delta function  $\delta(x)$  is approximated using the gaussian function  $1/\sqrt{2\pi\sigma^2} e^{-x^2/2\sigma^2}$ . So, with the gaussian broadening,  $A_{jk,1}(\omega)$  is computed as

$$A_{jk,1}(\omega) = \frac{1}{\sqrt{2\pi\sigma^2}} \sum_m \langle \Phi | c_j | m \rangle \langle m | c_k^\dagger | \Phi \rangle e^{-\frac{(\mathcal{E}_m - \mathcal{E}_\Phi - \omega)^2}{2\sigma^2}} \\ = \frac{1}{\sqrt{2\pi\sigma^2}} \langle \Phi | c_j e^{-(H - \mathcal{E}_\Phi - \omega)^2/2\sigma^2} c_k^\dagger | \Phi \rangle. \quad (\text{A4})$$

We consider the Green's function at  $\alpha$ . Then, like Eq. (5), we can represent  $A_{jk,1}(\omega)$  as

$$\begin{aligned} A_{jk,1}(\omega) &= \frac{1}{\sqrt{2\pi\sigma^2}} \frac{\tilde{A}_{jk,1}(\omega)}{\langle \Psi_\alpha | \Psi_\alpha \rangle}, \\ \tilde{A}_{jk,1}(\omega) &= \langle \Psi_\alpha | c_j e^{-(H_\alpha - E_\alpha - \omega)^2 / 2\sigma^2} c_k^\dagger | \Psi_\alpha \rangle. \end{aligned} \quad (\text{A5})$$

By fourier expansion of  $e^{-(H_\alpha - E_\alpha - \omega)^2}$ , we can compute  $\tilde{A}_{jk,1}$  like Eq. (6),

$$\tilde{A}_{jk,1}(\omega) = \frac{1}{N_\nu} \sum_{\nu} g_\alpha(c_j, c_k^\dagger, \mathbf{t}_\nu) e^{i\phi_\alpha(\mathbf{t}_\nu, \omega)}, \quad (\text{A6})$$

while  $g_\alpha(O_1, O_2, \mathbf{t}) = \langle \Phi_0 | e^{-iH_1 t_{2\alpha+1}} \dots e^{-iH_\alpha t_{\alpha+2}} O_1 e^{-iH_\alpha t_{\alpha+1}} O_2 e^{-iH_\alpha t_\alpha} \dots e^{-iH_1 t_1} | \Phi_0 \rangle$  and  $\phi_\alpha(\mathbf{t}, \omega) = \sum_{\alpha'=1}^{\alpha} E_{\alpha'}(t_{\alpha'} + t_{2\alpha+2-\alpha'}) + (E_\alpha + \omega)t_{\alpha+1}$ . Here,  $t_{\nu, \alpha+1} \sim \mathcal{N}(0, 1/\sigma)$  and  $t_{\nu, l} \sim \mathcal{N}(0, \beta)$  for all  $l \neq \alpha + 1$ . Since  $g_\alpha(O_1, O_2, \mathbf{t})$  is not dependent on  $\omega$ , we can compute  $A_{jk}(\omega)$  for any  $\omega$  by storing  $g_\alpha(c_j, c_k^\dagger, \mathbf{t}_\nu)$ .

### 3. Corrector for the energy difference

The energy difference formula, Eq. (7), can be derived as follows.

$$\begin{aligned} E_\alpha &= \frac{\langle \Phi_0 | \mathcal{P}_\alpha^\dagger H_\alpha \mathcal{P}_\alpha | \Phi_0 \rangle}{\langle \Phi_0 | \mathcal{P}_\alpha^\dagger \mathcal{P}_\alpha | \Phi_0 \rangle} \\ &= \frac{\langle \Phi_0 | \mathcal{P}_\alpha^\dagger | \Phi_\alpha \rangle \langle \Phi_\alpha | H_\alpha \mathcal{P}_{\alpha-1} | \Phi_0 \rangle}{\langle \Phi_0 | \mathcal{P}_\alpha^\dagger \mathcal{P}_\alpha | \Phi_0 \rangle} \\ &= \frac{\langle \Phi_0 | \mathcal{P}_\alpha^\dagger | \Phi_\alpha \rangle \langle \Phi_\alpha | (H_{\alpha-1} + h_{\alpha-1}) \mathcal{P}_{\alpha-1} | \Phi_0 \rangle}{\langle \Phi_0 | \mathcal{P}_\alpha^\dagger \mathcal{P}_\alpha | \Phi_0 \rangle} \\ &= E_{\alpha-1} + \frac{\langle \Psi_\alpha | \Phi_\alpha \rangle \langle \Phi_\alpha | h_{\alpha-1} | \Psi_{\alpha-1} \rangle}{\langle \Psi_\alpha | \Psi_\alpha \rangle}. \end{aligned} \quad (\text{A7})$$

By following same steps as obtaining Eq. (6), we obtain the Monte Carlo formula of the numerator  $\langle \Psi_\alpha | \Phi_\alpha \rangle \langle \Phi_\alpha | h_{\alpha-1} | \Psi_{\alpha-1} \rangle$ ,

$$\frac{1}{N_\nu} \sum_{\nu} \langle \Phi_0 | e^{-i(H_1 - E_1)t_{\nu, 2\alpha}} \dots e^{-i(H_\alpha - E_\alpha)t_{\nu, \alpha+1}} e^{-i(H_\alpha - E_\alpha)t_{\nu, \alpha}} h_{\alpha-1} \dots e^{-i(H_1 - E_1)t_{\nu, 1}} | \Phi_0 \rangle. \quad (\text{A8})$$

### 4. Computational cost of QZMC

This section provides details on the cost analysis of our method, which is briefly outlined in the main text. We consider the hamiltonian  $H(\lambda) = H_0 + \lambda H'$ . And we begin with  $|\Phi_0\rangle$ , an eigenstate of the  $H_0 = H(\lambda = 0)$  with eigenvalue  $E_0$ . For simplicity, we assume that  $|\Phi(\lambda)\rangle$ , which is adiabatically connected to  $|\Phi_0\rangle$ , is non-degenerate and has an eigenvalue  $E(\lambda)$  satisfying  $|E(\lambda) - \mathcal{E}_m(\lambda)| \geq \Delta_g$  for all eigenenergies of  $\mathcal{E}_m(\lambda)$  of  $H(\lambda)$  other than  $E(\lambda)$ . We then consider  $H_\alpha = H(\lambda_\alpha)$ ,  $\alpha = 1, \dots, N_\alpha$  with  $\lambda_\alpha = \alpha/N_\alpha$ , as in the main text. We denote  $E_\alpha = E(\lambda_\alpha)$ ,  $|\Phi_\alpha\rangle = |\Phi(\lambda_\alpha)\rangle$ .

a.  $N_\alpha$

First, we compute  $N_\alpha$  using exact projection. Utilizing perturbation theory [31], we have

$$\begin{aligned} \langle \Phi_\alpha | \Phi_{\alpha+1} \rangle &= \left( 1 - \frac{(\Delta\lambda)^2}{2} \sum_{m_\alpha \neq \Phi_\alpha} \frac{|\langle m_\alpha | H' | \Phi_\alpha \rangle|^2}{(E_\alpha - \mathcal{E}_{m,\alpha})^2} \right), \\ \langle m_\alpha | \Phi_{\alpha+1} \rangle &= \Delta\lambda \frac{\langle m_\alpha | H' | \Phi_\alpha \rangle}{E_\alpha - \mathcal{E}_{m,\alpha}} \text{ for } m_\alpha \neq \Phi_\alpha, \end{aligned} \quad (\text{A9})$$

up to the leading order of  $\Delta\lambda = \lambda_{\alpha+1} - \lambda_\alpha$ . Here,  $|m_\alpha\rangle$  represent an eigenstate of  $H_\alpha$  with an eigenvalue of  $\mathcal{E}_{m,\alpha}$ . However,

$$\sum_{m_\alpha \neq \Phi_\alpha} \frac{|\langle m_\alpha | H' | \Phi_\alpha \rangle|^2}{(E_\alpha - \mathcal{E}_{m,\alpha})^2} \leq \frac{1}{\Delta_g^2} \|H'\|^2. \quad (\text{A10})$$

Here, we employ the matrix norm induced by vector 2-norm [30],  $\|A\| = \sup_{\|x\|=1} \|Ax\|$ . Combining Eq. (A9) and Eq. (A10), we obtain

$$\langle \Psi_\alpha | \Psi_\alpha \rangle = \prod_{a=1}^{\alpha} |\langle \Phi_{a-1} | \Phi_a \rangle|^2 \geq 1 - \frac{\|H'\|^2}{\Delta_g^2} \frac{1}{N_\alpha}. \quad (\text{A11})$$

Thus, we have  $\|\Psi_\alpha\|^2 \geq 1 - \eta_0$  for all  $\alpha$  by setting

$$N_\alpha \geq \frac{\|H'\|^2}{\Delta_g^2} \frac{1}{\eta_0}. \quad (\text{A12})$$

For the ground state, we can make this bound more tight because

$$\begin{aligned} \langle \Phi_\alpha | \Phi_{\alpha+1} \rangle &= \left( 1 - \frac{(\Delta\lambda)^2}{2} \sum_{m_\alpha \neq \Phi_\alpha} \frac{|\langle m_\alpha | H' | \Phi_\alpha \rangle|^2}{(E_\alpha - \mathcal{E}_{m,\alpha})^2} \right) \\ &\geq 1 - \frac{(\Delta\lambda)^2}{4} \frac{E''(\lambda_\alpha)}{\Delta_g}. \end{aligned} \quad (\text{A13})$$

Here,  $E''(\lambda_\alpha)$  is the second derivative of  $E(\lambda)$  at  $\lambda_\alpha$ . So,

$$\begin{aligned} \langle \Psi_\alpha | \Psi_\alpha \rangle &\geq 1 - \frac{1}{\Delta_g} \sum_{\alpha} \frac{E''(\lambda_\alpha)}{2N_\alpha^2} \\ &= 1 - \frac{1}{\Delta_g} \frac{(E'(1) - E'(0))}{2N_\alpha} + \mathcal{O}\left(\frac{1}{N_\alpha^2}\right). \end{aligned} \quad (\text{A14})$$

As  $E'(\lambda) = \langle \Phi(\lambda) | H' | \Phi(\lambda) \rangle \leq \|H'\|$ , we conclude

$$\langle \Psi_\alpha | \Psi_\alpha \rangle \geq 1 - \frac{\|H'\|}{\Delta_g} \frac{1}{N_\alpha}, \quad (\text{A15})$$

up to the first order of  $1/N_\alpha$ . So, for the ground state, it is enough to have

$$N_\alpha \geq \frac{\|H'\|}{\Delta_g} \frac{1}{\eta_0}, \quad (\text{A16})$$

to get  $\|\Psi_\alpha\|^2 \geq 1 - \eta_0$ .

b.  $\beta$

The impact of finite  $\beta$  on the projected state is described by

$$|\delta\Psi_\alpha^\beta\rangle = (\mathcal{P}_\alpha^\beta - \mathcal{P}_\alpha)|\Phi_0\rangle. \quad (\text{A17})$$

Here, we show

$$\|\delta\Psi_\alpha^\beta\| \leq \frac{\alpha}{N_\alpha} e^{-\beta^2 \Delta_g^2 / 2} \frac{\|H'\|}{\Delta_g} \quad (\text{A18})$$

inductively, where  $\|\delta\Psi_\alpha^\beta\|^2 = \langle \delta\Psi_\alpha^\beta | \delta\Psi_\alpha^\beta \rangle$ . First, we address the case of  $\alpha = 1$ . Employing the perturbation approach as in Eq.(A9), we obtain

$$\begin{aligned} \|\delta\Psi_1^\beta\|^2 &= \langle \Phi_0 | (P_{H_1}^\beta(E_1) - |\Phi_1\rangle\langle\Phi_1|)^2 | \Phi_0 \rangle \\ &= (\Delta\lambda)^2 \sum_{m_1 \neq \Phi_1} e^{-\beta^2(\mathcal{E}_{m,1} - E_1)^2} \frac{|\langle \Phi_1 | H' | m_1 \rangle|^2}{(\mathcal{E}_{m,1} - E_1)^2} \\ &\leq (\Delta\lambda)^2 e^{-\beta^2 \Delta_g^2} \frac{\|H'\|^2}{\Delta_g^2} \end{aligned} \quad (\text{A19})$$

So,  $\|\delta\Psi_1^\beta\| \leq \frac{1}{N_\alpha} e^{-\beta^2 \Delta_g^2 / 2} \frac{\|H'\|}{\Delta_g}$ . Suppose for  $\alpha$ ,  $\|\delta\Psi_\alpha^\beta\| \leq \frac{\alpha}{N_\alpha} e^{-\beta^2 \Delta_g^2 / 2} \frac{\|H'\|}{\Delta_g}$ . Then,

$$\begin{aligned} |\delta\Psi_{\alpha+1}^\beta\rangle &= (P_{\alpha+1}^\beta - |\Phi_{\alpha+1}\rangle\langle\Phi_{\alpha+1}|) |\Psi_\alpha\rangle \\ &\quad + P_{\alpha+1}^\beta |\delta\Psi_\alpha^\beta\rangle. \end{aligned} \quad (\text{A20})$$

For simplicity, we expressed  $P_{\alpha+1}^\beta = P_{H_{\alpha+1}}^\beta(E_{\alpha+1})$ . Thus,

$$\begin{aligned} \|\delta\Psi_{\alpha+1}^\beta\|^2 &= \langle \Psi_\alpha | (P_{\alpha+1}^\beta - |\Phi_{\alpha+1}\rangle\langle\Phi_{\alpha+1}|)^2 | \Psi_\alpha \rangle \\ &\quad + \langle \Psi_\alpha | (P_{\alpha+1}^\beta - |\Phi_{\alpha+1}\rangle\langle\Phi_{\alpha+1}|) P_{\alpha+1}^\beta |\delta\Psi_\alpha^\beta\rangle \\ &\quad + \langle \delta\Psi_\alpha^\beta | P_{\alpha+1}^\beta (P_{\alpha+1}^\beta - |\Phi_{\alpha+1}\rangle\langle\Phi_{\alpha+1}|) | \Psi_\alpha \rangle \\ &\quad + \langle \delta\Psi_\alpha^\beta | (P_{\alpha+1}^\beta)^2 | \delta\Psi_\alpha^\beta \rangle. \end{aligned} \quad (\text{A21})$$

The first term is smaller than  $(\Delta\lambda)^2 e^{-\beta^2 \Delta_g^2} \frac{\|H'\|^2}{\Delta_g^2}$  by following the same procedure as with Eq. (A19). And the last term is smaller than  $\|\delta\Psi_\alpha^\beta\|^2 \leq \frac{\alpha^2}{N_\alpha^2} e^{-\beta^2 \Delta_g^2} \frac{\|H'\|^2}{\Delta_g^2}$  since  $P_\alpha^\beta$  has eigenvalues smaller than 1. Consider the second term. Then,

$$\begin{aligned} &|\langle \Psi_\alpha | (P_{\alpha+1}^\beta - |\Phi_{\alpha+1}\rangle\langle\Phi_{\alpha+1}|) P_{\alpha+1}^\beta |\delta\Psi_\alpha^\beta\rangle| \\ &\leq \Delta\lambda \frac{e^{-\beta^2 \Delta_g^2}}{\Delta_g} \sum_{\substack{m_{\alpha+1} \\ \neq \Phi_{\alpha+1}}} |\langle \Phi_{\alpha+1} | H' | m_{\alpha+1} \rangle| |\langle m_{\alpha+1} | \delta\Psi_\alpha^\beta \rangle| \\ &\leq \Delta\lambda \frac{e^{-\beta^2 \Delta_g^2}}{\Delta_g} \|H' | \Phi_{\alpha+1} \rangle\| \|\delta\Psi_\alpha^\beta\| \\ &\leq \Delta\lambda \frac{e^{-\beta^2 \Delta_g^2}}{\Delta_g} \|H'\| \|\delta\Psi_\alpha^\beta\| \\ &\leq \Delta\lambda \frac{\alpha}{N_\alpha} e^{-\beta^2 \Delta_g^2} \frac{\|H'\|^2}{\Delta_g^2}. \end{aligned} \quad (\text{A22})$$

Similar argument provides the same bound for the third term. By using  $\Delta\alpha = 1/N_\alpha$ , we have

$$\|\delta\Psi_{\alpha+1}^\beta\|^2 \leq \frac{(\alpha+1)^2}{N_\alpha^2} e^{-\beta^2 \Delta_g^2} \frac{\|H'\|^2}{\Delta_g^2}, \quad (\text{A23})$$

which proves Eq. (A18). So,  $|\langle \Psi_\alpha | \Psi_\alpha \rangle - \langle \Psi_\alpha^\beta | \Psi_\alpha^\beta \rangle|$  becomes smaller than  $\delta\eta$  by using

$$\beta \geq \frac{1}{\Delta_g} \sqrt{2 \log \left( \frac{\|H'\|}{\Delta_g} \frac{2}{\delta\eta} \right)}. \quad (\text{A24})$$

If we are interested in the expectation value of the observable  $O$ ,  $\langle \Psi_\alpha^\beta | O | \Psi_\alpha^\beta \rangle$  has an error of

$$\begin{aligned} \delta\langle \Psi_\alpha^\beta | O | \Psi_\alpha^\beta \rangle &= \langle \delta\Psi_\alpha^\beta | O | \Psi_\alpha \rangle + \langle \Psi_\alpha | O | \delta\Psi_\alpha^\beta \rangle \\ &\quad + \langle \delta\Psi_\alpha^\beta | O | \delta\Psi_\alpha^\beta \rangle. \end{aligned} \quad (\text{A25})$$

which is smaller than

$$2\|\delta\Psi_\alpha^\beta\| \|O\| + \|\delta\Psi_\alpha^\beta\|^2 \|O\|. \quad (\text{A26})$$

By considering error up to the first order of  $\|\delta\Psi_\alpha^\beta\|$ , we have

$$\delta\langle \Psi_\alpha^\beta | O | \Psi_\alpha^\beta \rangle \leq 2\|\delta\Psi_\alpha^\beta\| \|O\|. \quad (\text{A27})$$

Then, the error of the expectation value  $\langle \Psi_\alpha^\beta | O | \Psi_\alpha^\beta \rangle / \langle \Psi_\alpha^\beta | \Psi_\alpha^\beta \rangle$  is estimated by

$$\begin{aligned} \delta \left( \frac{\langle \Psi_\alpha^\beta | O | \Psi_\alpha^\beta \rangle}{\langle \Psi_\alpha^\beta | \Psi_\alpha^\beta \rangle} \right) &= \frac{\delta\langle \Psi_\alpha^\beta | O | \Psi_\alpha^\beta \rangle}{\langle \Psi_\alpha^\beta | \Psi_\alpha^\beta \rangle} + \frac{\langle \Psi_\alpha | O | \Psi_\alpha \rangle}{\langle \Psi_\alpha | \Psi_\alpha \rangle^2} \delta\langle \Psi_\alpha^\beta | \Psi_\alpha^\beta \rangle \\ &\leq 4 \frac{\|\delta\Psi_\alpha^\beta\|}{\langle \Psi_\alpha | \Psi_\alpha \rangle} \|O\|, \end{aligned} \quad (\text{A28})$$

because  $\langle \Psi_\alpha | O | \Psi_\alpha \rangle / \langle \Psi_\alpha | \Psi_\alpha \rangle \leq \|O\|$ . So, if  $\langle \Psi_\alpha | \Psi_\alpha \rangle \geq 1 - \eta$ ,  $\langle O \rangle$  can be estimated within an error of  $\epsilon$  by using

$$\beta \geq \frac{1}{\Delta_g} \sqrt{2 \log \left( \frac{\|H'\|}{\Delta_g} \frac{4\|O\|}{1 - \eta} \frac{1}{\epsilon} \right)} \quad (\text{A29})$$

The energy estimator in Eq. (7) is a slightly different case since we are computing the energy difference at each  $\alpha$ . With finite  $\beta$ , the numerator in Eq. (7) have an error of

$$\begin{aligned} &\langle \Psi_\alpha^\beta | P_{\alpha+1}^\beta P_{\alpha+1}^\beta (H_{\alpha+1} - E_{\alpha+1}) | \Psi_\alpha^\beta \rangle \\ &\quad - \langle \Psi_\alpha^\beta | P_{\alpha+1}^\beta P_{\alpha+1}^\beta (H_\alpha - E_\alpha) | \Psi_\alpha^\beta \rangle. \end{aligned} \quad (\text{A30})$$

Here, we considered error at  $\alpha + 1$  in Eq. (7) instead of  $\alpha$  for the notational simplicity. Up to first order of  $\Delta\lambda$  and  $\|\delta\Psi_\alpha^\beta\|$ , above equation is equal to

$$\begin{aligned} &\langle \delta\Psi_\alpha^\beta | P_{\alpha+1}^\beta P_{\alpha+1}^\beta (H_{\alpha+1} - E_{\alpha+1}) | \Psi_\alpha^\beta \rangle \\ &\quad - \langle \delta\Psi_\alpha^\beta | P_{\alpha+1}^\beta P_{\alpha+1}^\beta (H_\alpha - E_\alpha) | \Psi_\alpha^\beta \rangle \\ &+ \langle \Psi_\alpha^\beta | P_{\alpha+1}^\beta P_{\alpha+1}^\beta (H_{\alpha+1} - E_{\alpha+1}) | \delta\Psi_\alpha^\beta \rangle \\ &\quad - \langle \Psi_\alpha^\beta | P_{\alpha+1}^\beta P_{\alpha+1}^\beta (H_\alpha - E_\alpha) | \delta\Psi_\alpha^\beta \rangle. \end{aligned} \quad (\text{A31})$$

By using  $H_{\alpha+1} - H_\alpha = \Delta\lambda H'$  and  $E_{\alpha+1} - E_\alpha = \Delta\lambda E'_\alpha + \mathcal{O}(\Delta\lambda^2)$ , Eq. (A31) is equal to

$$\begin{aligned} & \Delta\lambda (\langle \delta\Psi_\alpha^\beta | P_{\alpha+1}^\beta P_{\alpha+1}^\beta (H' - E'_\alpha) | \Psi_\alpha \rangle \\ & + \langle \Psi_\alpha | P_{\alpha+1}^\beta P_{\alpha+1}^\beta (H' - E'_\alpha) | \delta\Psi_\alpha^\beta \rangle), \end{aligned} \quad (\text{A32})$$

which is smaller than

$$4\Delta\lambda \|\delta\Psi_\alpha^\beta\| \|H'\|, \quad (\text{A33})$$

as  $E'_\alpha \leq \|H'\|$ . If  $\|\Psi_\alpha^\beta\|^2 \geq 1 - \eta$ , each energy difference estimator has the error no greater than

$$4\Delta\lambda \frac{\|\delta\Psi_\alpha^\beta\| \|H'\|}{1 - \eta} \leq 4 \frac{\alpha}{N_\alpha^2} e^{-\beta^2 \Delta_g^2 / 2} \frac{\|H'\|^2}{\Delta_g} \frac{1}{1 - \eta}. \quad (\text{A34})$$

Thus, the energy estimation  $E_\alpha$  has the error bound of

$$2 \frac{\alpha(\alpha - 1)}{N_\alpha^2} e^{-\beta^2 \Delta_g^2 / 2} \frac{\|H'\|^2}{\Delta_g} \frac{1}{1 - \eta}, \quad (\text{A35})$$

which increases as  $\alpha$  increase and is smaller than  $2e^{-\beta^2 \Delta_g^2 / 2} \frac{\|H'\|^2}{\Delta_g} \frac{1}{1 - \eta}$ . So, we can compute the energy within an error of  $\epsilon$  by using

$$\beta \geq \frac{1}{\Delta_g} \sqrt{2 \log \left( \frac{2\|H'\|^2}{\Delta_g} \frac{1}{1 - \eta} \frac{1}{\epsilon} \right)}. \quad (\text{A36})$$

#### c. $N_\nu$

Consider a random variable  $\mathbf{t}$  with a continuous probability distribution  $g(\mathbf{t})$ . The expectation value of  $x(\mathbf{t})$  is given by

$$\mathbb{E}[x] = \int x(\mathbf{t})g(\mathbf{t})d\mathbf{t}. \quad (\text{A37})$$

The variance of the  $x$  is calculated as

$$\text{Var}[x] = \mathbb{E}[x^2] - (\mathbb{E}[x])^2. \quad (\text{A38})$$

If  $|x(\mathbf{t})| \leq L$  for all  $\mathbf{t}$ , we have  $\mathbb{E}[x^2] \leq L^2$ , which gives

$$\sigma_x^2 = \text{Var}[x] \leq L^2 - (\mathbb{E}[x])^2 \leq L^2. \quad (\text{A39})$$

Consequently, if we generate  $N_\nu$  samples of  $\mathbf{t}$  and use the average of  $x(\mathbf{t})$  as our estimator  $\bar{x}$  of  $\mathbb{E}[x]$ , standard error  $\sigma_{\bar{x}}$  of  $\bar{x}$  is bounded by  $\frac{L}{\sqrt{N_\nu}}$  [29]. This discussion extends to for Eq. (6) with  $L = \|A\|$ . The observable expectation Eq. (5) can be seen as  $\bar{x}$  divided by  $\bar{y}$ , where  $|x(\mathbf{t})| \leq L$  and  $|y(\mathbf{t})| \leq 1$ . Then, by using the the delta method [29] and independent sampling of  $\mathbf{t}$  for  $\bar{x}$  and  $\bar{y}$ , the variance  $\sigma_{\bar{x}/\bar{y}}^2$  of  $\bar{x}/\bar{y}$  is estimated as

$$\sigma_{\bar{x}/\bar{y}}^2 = \frac{1}{\bar{y}^2} \left( \sigma_{\bar{x}}^2 + \frac{\bar{x}^2}{\bar{y}^2} \sigma_{\bar{y}}^2 \right) \leq \frac{L^2}{N_\nu \bar{y}^2} \left( 1 + \frac{1}{\bar{y}^2} \right). \quad (\text{A40})$$

Therefore, the standard error  $\sigma_{\langle O \rangle_\alpha}$  of  $\langle O \rangle_\alpha$  becomes

$$\sigma_{\langle O \rangle_\alpha} \leq \frac{\|O\|}{\sqrt{N_\nu}} \frac{1}{\langle \Psi_\alpha^\beta | \Psi_\alpha^\beta \rangle} \sqrt{1 + \frac{1}{\langle \Psi_\alpha^\beta | \Psi_\alpha^\beta \rangle^2}}. \quad (\text{A41})$$

Similarly, the energy difference calculated by Eq. (A8) has a standard error of

$$\sigma_{E_\alpha - E_{\alpha-1}} \leq \Delta\lambda \frac{\|H'\|}{\sqrt{N_\nu}} \frac{1}{\langle \Psi_\alpha^\beta | \Psi_\alpha^\beta \rangle} \sqrt{1 + \frac{1}{\langle \Psi_\alpha^\beta | \Psi_\alpha^\beta \rangle^2}}. \quad (\text{A42})$$

#### d. The number of shots, $N_s$

In real quantum computers, the estimation of unitary expectation value involves with a finite number  $N_s$  of repetitions of the same circuits, commonly referred as shots. This introduces statistical errors with a standard deviation of  $1/\sqrt{N_s}$  to each measurement. Consequently, when measuring observable  $\langle O \rangle$  using the pauli string expansion, the finite number of shots modifies  $\|O\|$  in Eq. (A41) to  $\|O\| + \sqrt{\sum_\gamma o_\gamma^2 / N_s}$ , where  $O = \sum_\gamma o_\gamma P_\gamma$  represents a pauli string expansion of  $O$ . Similarly, with finite number of shots,  $\|H'\| \rightarrow \|H'\| + \sqrt{\sum_\gamma w_\gamma^2 / N_s}$  in Eq. (A42). Here,  $H' = \sum_\gamma w_\gamma P_\gamma$  stands as a pauli string expansion of  $H'$ .

#### e. Cost of the energy estimation

In this section, we explore the computational cost of obtaining the energy eigenvalue with an additive error of  $\epsilon$  by determining suitable computational parameters  $N_\alpha$ ,  $\beta$ , and  $N_\nu$ . Similarly, complexities for observable calculations can be derived. The computational cost of the quantum algorithm is mainly influenced by the circuit depth and the number of repetitions. To quantify the circuit depth, we examine the distribution of the consecutive time evolution length  $L_\nu = |t_{\nu,1}| + \dots + |t_{\nu,2N_\alpha}|$ . Since each  $|t_{\nu,1}|, \dots, |t_{\nu,2N_\alpha}|$  follows a half-normal distribution with a mean of  $\beta\sqrt{2/\pi}$  and a standard deviation of  $\beta\sqrt{1 - 2/\pi}$ ,  $L_\nu$  has a mean  $2N_\alpha\beta\sqrt{2/\pi}$  and a standard deviation of  $\sqrt{2N_\alpha}\beta\sqrt{1 - 2/\pi}$ . As a measure of the maximum time evolution length, we employ 90th percentile,  $C_{90}N_\alpha\beta$ , where the probability of  $L_\nu$  being smaller than  $C_{90}N_\alpha\beta$  is 90%.  $C_{90}$  is numerically determined by testing the cumulative distribution of  $L_\nu$ , and it monotonically decreases as  $N_\alpha$  increases. For  $N_\alpha = 1$ ,  $C_{90} = 2.7545$ , which reduces to 2.0978 at  $N_\alpha = 5$ , and eventually approaches  $2\sqrt{2/\pi}$  as  $N_\alpha \rightarrow \infty$ .

Then,  $\beta$  and  $N_\alpha$  determines the circuit depth. We find appropriate values for  $\beta$  and  $N_\alpha$  by ensuring that  $\langle \Psi_\alpha^\beta | \Psi_\alpha^\beta \rangle \geq 1 - \eta$ , where  $\eta = 0.5$ , in order to limit error amplification. To achieve this, we set  $\eta_0 = 0.4$  in Eq. (A16) and  $\delta\eta$  in Eq. (A24) to 0.1, resulting in  $\eta = \eta_0 + \delta\eta = 0.5$ . Considering the ground state energy error of  $\epsilon$  in Eq. (A36), this gives

$$N_\alpha\beta \geq 2.5 \frac{\|H'\|}{\Delta_g^2} \sqrt{2 \log \left( \max \left( \frac{4\|H'\|^2}{\Delta_g} \frac{1}{\epsilon}, \frac{20\|H'\|}{\Delta_g} \right) \right)}. \quad (\text{A43})$$

So, in terms of  $n$ , the number of qubits, we have the maximum

evolution time of

$$C_{90}N_{\alpha}\beta = \mathcal{O}(\Delta_g^{-2} \text{poly}(n))\sqrt{\log(\mathcal{O}(\Delta_g^{-1}\epsilon^{-1} \text{poly}(n)))}. \quad (\text{A44})$$

From Eq. (A12), we have additional  $\Delta^{-1}$  dependence for the non-ground state.

Next, we consider the number of repetitions. Given that we compute  $N_{\nu}$  circuits with  $N_s$  shots each, the total number of repetitions is  $N_{\nu}N_s$ . Utilizing Eq. (A42) with finite number of shots and  $\langle \Psi_{\alpha}^{\beta} | \Psi_{\alpha}^{\beta} \rangle \geq 1 - \eta = 0.5$ , we can compute Eq. (7) within an error of  $\epsilon$  with the Monte Carlo samples

$$N_{\nu} \geq \left( \|H'\| + \frac{\sqrt{\sum_{\gamma} w_{\gamma}^2}}{\sqrt{N_s}} \right)^2 \frac{20}{\epsilon^2} \quad (\text{A45})$$

for each  $\alpha$ . By fixing  $N_s$ , we find  $N_{\nu} = \mathcal{O}(\epsilon^{-2} \text{poly}(n))$ , as  $\|H'\|^2$  and  $\sum_{\gamma} w_{\gamma}^2$  are  $\mathcal{O}(\text{poly}(n))$ . Consequently, the total number of repetitions required to obtain the energy eigenvalue within an error of  $\epsilon$  is

$$N_{\nu}N_s = \mathcal{O}(\epsilon^{-2} \text{poly}(n)). \quad (\text{A46})$$

### 5. The effect of the inaccurate energy eigenvalues

In practical calculations, we encounter a finite error  $\delta$  in energy estimation. The effect of this energy error is  $e^{-\beta^2\delta^2}$  for each projection. However, this effect cancels out for the calculation of the expectation values and the energy difference formula. Thus, one should only consider that

$$e^{-2N_{\alpha}\beta^2\delta^2} \quad (\text{A47})$$

is not too small to completely destroy  $\langle \Psi_{\alpha}^{\beta} | \Psi_{\alpha}^{\beta} \rangle$ . To ensure that this value is greater than  $1/2$ , we require  $\beta$  to satisfy

$$\beta \leq \frac{1}{\delta} \sqrt{\frac{\log 2}{2N_{\alpha}}}. \quad (\text{A48})$$

### 6. Quantum Circuits for QZMC

We illustrate several quantum circuits utilized in the quantum Zeno Monte Carlo (QZMC) method. Figure 7 depicts the QZMC circuits employing controlled time-evolution. If noise is too large so that the noise that (a)-(c) experience are significantly different to each other, we can use (d) for the calculation of  $\langle \Psi | \Psi \rangle$  instead of (a) to mitigate the influence of the noise. QZMC with the circuits shown in Fig. 7 is general and applicable for any Hamiltonian. However, it may suffer from substantial device noise due to numerous controlled-time evolutions. To circumvent this, we can adopt the quantum circuits depicted in Figure 8. This approach eliminates the need for controlled time-evolution when a common eigenstate  $|\Phi_{\text{ref}}\rangle$  exists for  $H_1, \dots, H_{N_{\alpha}}$ . While this appears to be a stringent restriction, many practical physical

and chemical systems possess such a common eigenstate, such as the vacuum. For the Green's function calculation, we have to compute  $g_{\alpha}$  in Eq. (A6). Through the pauli string decomposition, this translates into a weighted sum of  $\langle \Phi_0 | e^{-iH_1 t_{2\alpha+1}} \dots e^{-iH_{\alpha} t_{\alpha+2}} P_{\gamma} e^{-iH_{\alpha} t_{\alpha+1}} P_{\gamma'} e^{-iH_{\alpha} t_{\alpha}} \dots e^{-iH_1 t_1} | \Phi_0 \rangle$ . Therefore, the Green's function calculation can be executed using the quantum circuits depicted in Figure 9.

## Appendix B: Details of NISQ calculations

In this section, we describe details of NISQ simulations considered in the main text. Throughout the NISQ simulations, we used  $N_s = 4000$ .

### 1. Compressed quantum circuit

First, we present the compressed circuits for the 1 and 2 qubit systems, used for computations in Fig. 2-3. Because any 1 and 2 qubit unitary can be represented with a few operations [50], we can use compressed circuits Figure 10 instead of Fig. 7 or Fig. 8 for those cases. For the 1-qubit system, parameters  $\theta$  for the unitary matrix  $U$  is found from [50]

$$U = e^{i\theta_4} \begin{bmatrix} \cos(\theta_1/2) & -\sin(\theta_1/2)e^{i\theta_3} \\ \sin(\theta_1/2)e^{i\theta_2} & \cos(\theta_1/2)e^{i(\theta_2+\theta_3)} \end{bmatrix}. \quad (\text{B1})$$

For the 2-qubit system, we used the two-qubit Weyl decomposition [51] as implemented in the qiskit.

### 2. One-qubit system

In the main text, we investigated the one-qubit system described by the Hamiltonian  $H(\lambda) = X/2 + (2\lambda - 1)Z$ , traversing from  $\lambda = 0$  to  $\lambda = 1$  via a discrete path with  $\lambda_{\alpha} = \alpha/N_{\alpha}$ . Here, with noiseless simulator, we assess the parameter dependencies of QZMC by varying  $N_{\alpha}$  and  $\beta$ , and also evaluating the impact of finite Trotterization steps. Figure 11 illustrates these dependencies for  $\langle \Psi | \Psi \rangle$  and the ground state energy  $E$  of  $H(\lambda = 1)$ . (a) and (b) of Fig. 11 demonstrate the  $\beta$  dependence. This reveals an increasing accuracy with  $\beta$  until  $\beta = 10$ . Large error for  $\beta > 10$  can be understood from Eq. (A47). Next, (c) and (d) depict the variation of  $\langle \Psi | \Psi \rangle$  and  $E$  with  $N_{\alpha}$ , showcasing convergence to exact values as  $N_{\alpha}$  increases, with  $E$  attaining accuracy as soon as  $\langle \Psi | \Psi \rangle$  takes a non-trivial value, at  $N_{\alpha} = 5$ . Finally, (e)-(f) display the results with Trotterization, where the Trotterized time evolution  $U(\lambda, \tau, N_T)$  for  $H(\lambda)$  is defined as

$$U(\lambda, \tau, N_T) = \prod_l^{N_T} e^{-i\Delta\tau X/2} e^{-i\Delta\tau(2\lambda-1)Z} \quad (\text{B2})$$

with  $\Delta\tau = \tau/N_T$ . With increasing  $N_T$ ,  $\langle \Psi | \Psi \rangle$  converges to its exact value, while  $E$  converges to the exact values more rapidly, indicating the noise resilience of  $E$  in the presence of inaccurate time-evolution.

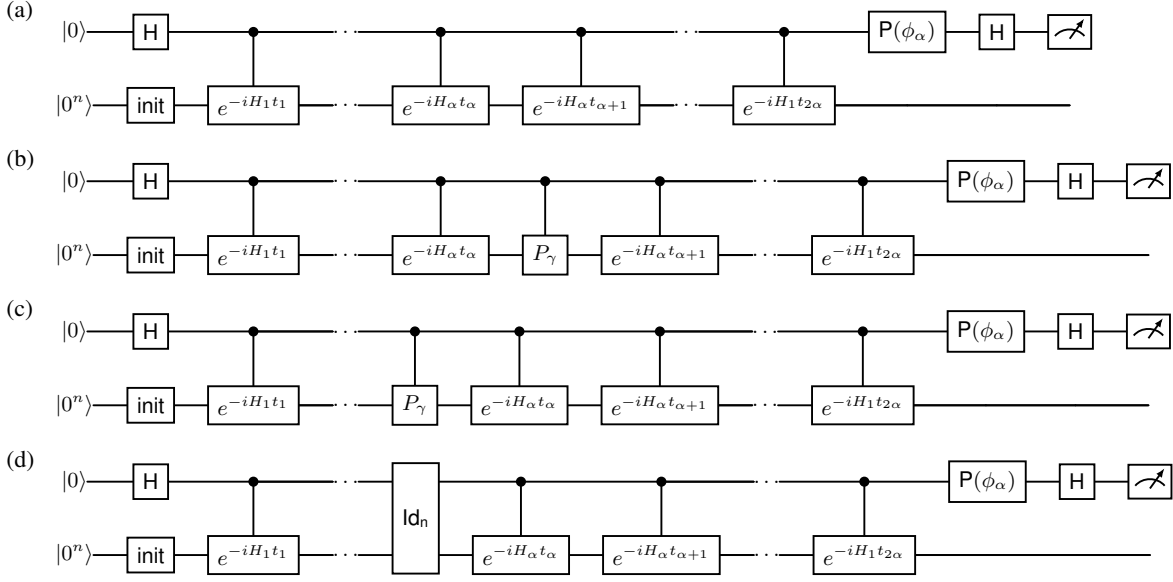


Figure 7. Quantum circuits for QZMC without a reference state. (a) is the circuit for  $\langle \Psi | \Psi \rangle$ , (b) for  $\langle \Psi | O | \Psi \rangle$ , and (c) for  $\langle \Psi_\alpha | \Phi_\alpha \rangle \langle \Phi_\alpha | h_{\alpha-1} | \Psi_{\alpha-1} \rangle$ . The noise effect difference in  $\langle \Psi | \Psi \rangle$  and  $\langle \Psi_\alpha | \Phi_\alpha \rangle \langle \Phi_\alpha | h_{\alpha-1} | \Psi_{\alpha-1} \rangle$  can be reduced by using the circuit (d), which contains noisy identity that mimics the noise effect of controlled- $P_\gamma$ , instead of (a). The circuit `init` refers the circuit that transforms  $|0^n\rangle$  to  $|\Phi_0\rangle$ .

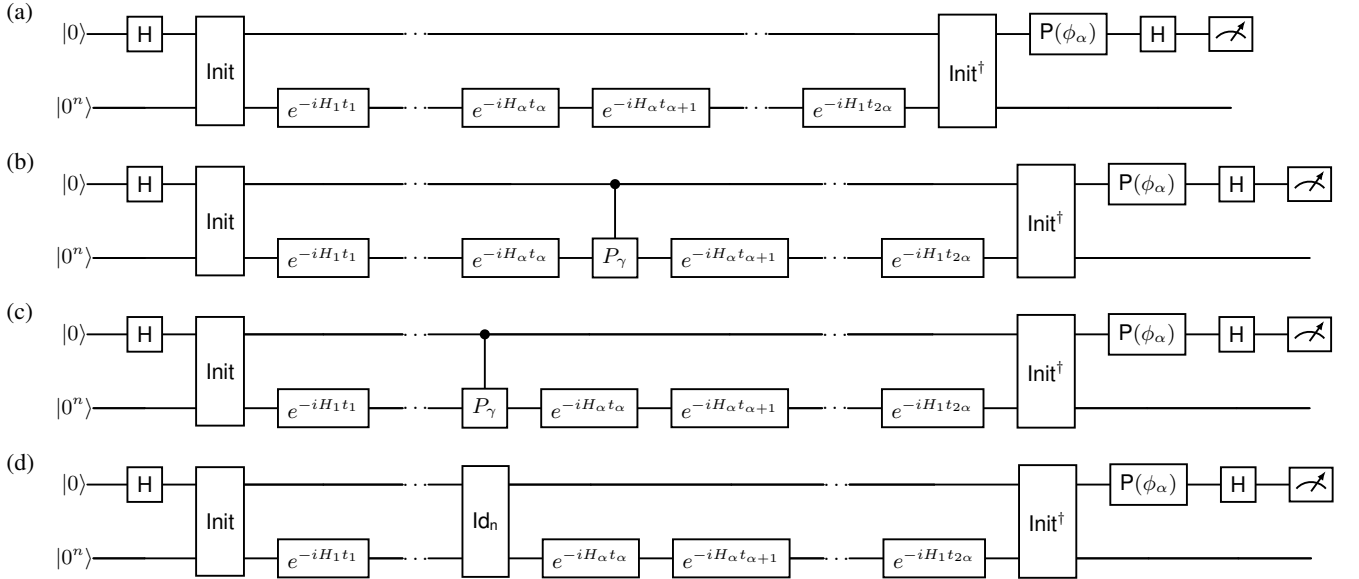


Figure 8. Quantum circuits for QZMC with a reference state. (a) is the circuit for  $\langle \Psi | \Psi \rangle$ , (b) for  $\langle \Psi | O | \Psi \rangle$ , and (c) for  $\langle \Psi_\alpha | \Phi_\alpha \rangle \langle \Phi_\alpha | h_{\alpha-1} | \Psi_{\alpha-1} \rangle$ . (d) is the circuit for the  $\langle \Psi | \Psi \rangle$  that includes noisy identity `Idn`, making noise effect on  $\langle \Psi | \Psi \rangle$  and  $\langle \Psi_\alpha | \Phi_\alpha \rangle \langle \Phi_\alpha | h_{\alpha-1} | \Psi_{\alpha-1} \rangle$  similar to each other. The circuit `init` transforms  $|0^n\rangle$  to a reference state  $|\Phi_{\text{ref}}\rangle$  if the control qubit is at  $|0\rangle$ , and  $|0^n\rangle$  to  $|\Phi_0\rangle$  if the control qubit is at  $|1\rangle$ .

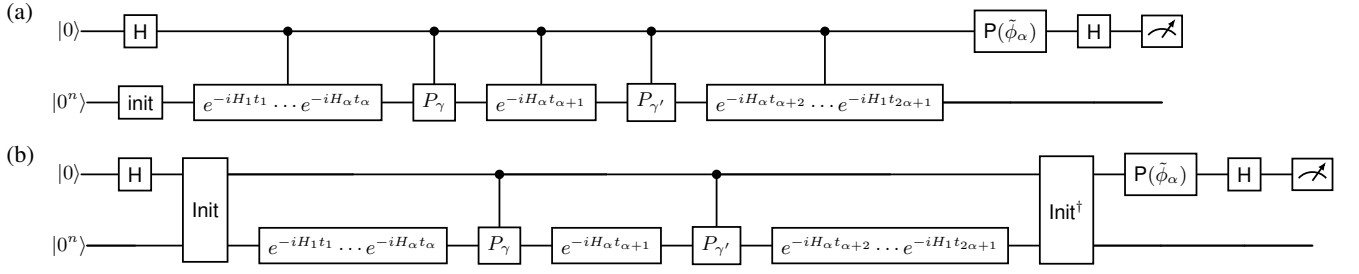


Figure 9. Quantum circuits for Green's function. (a) is the circuit without a reference state, (b) is the circuit with a reference state.  $\tilde{\phi}_\alpha = \phi_\alpha$  for a real part,  $\tilde{\phi}_\alpha = \phi_\alpha - \pi/2$  for an imaginary part.

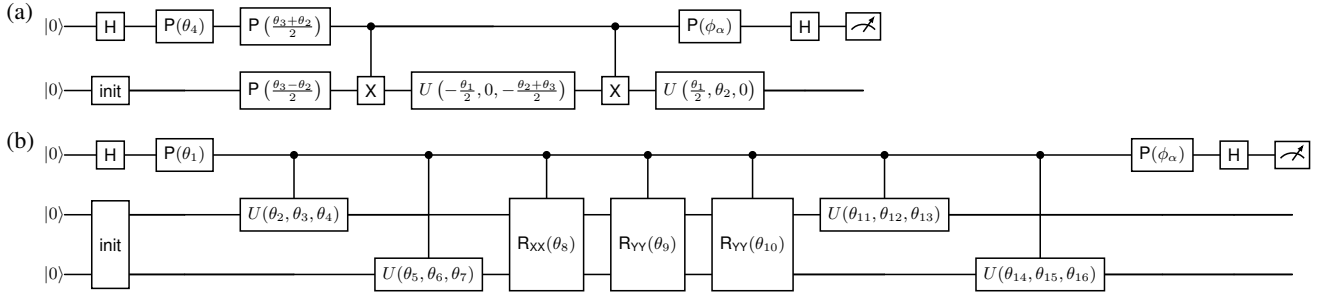


Figure 10. Quantum circuits for QZMC that uses 1 and 2 qubit circuit compression (a) is the compressed circuit for 1-qubit systems, and (b) is the compressed circuit for 2-qubit systems.

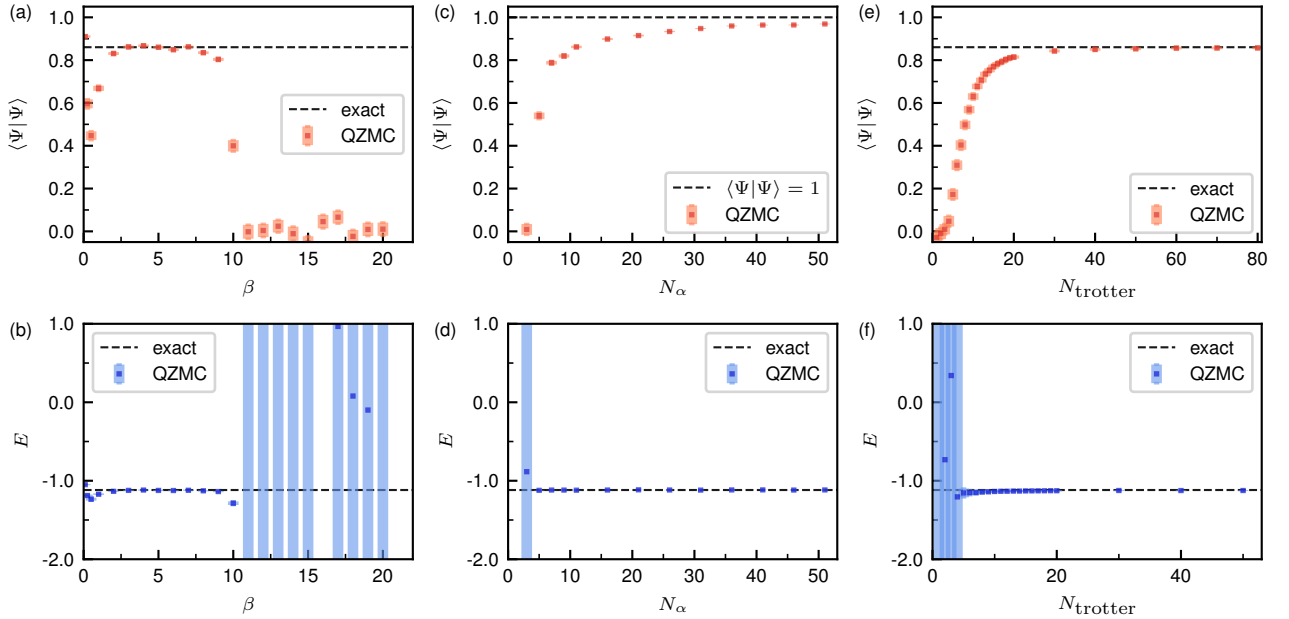


Figure 11. Parameter dependence of QZMC applied on the one-qubit system.  $\beta$  dependence of (a)  $\langle \Psi | \Psi \rangle$  and (b)  $E$ ,  $N_\alpha$  dependence of (c)  $\langle \Psi | \Psi \rangle$  and (d)  $E$ , and  $N_T$  dependence of (e)  $\langle \Psi | \Psi \rangle^2$  and (f)  $E$  for a ground state are plotted. In (a) and (b),  $N_\alpha = 10$  and we used the exact time evolution. For (c) and (d), we used  $\beta = 5$  and the exact time evolution. And (e) and (f) are computed with  $\beta = 5$  and  $N_\alpha = 10$ . In this figure, squares represents data points and shaded region is the numerically estimated error-bar. Here, We fixed  $N_\nu = 400$ .

### 3. Hubbard dimer

Here, we demonstrate the application of QZMC to the Hubbard dimer using Trotterized time evolution on an *ibm perth* quantum computer. We focus solely on the ground state for simplicity, employing second-order Trotterization for the time evolution. For  $H = H_1 + H_2$ , the second order Trotterized time evolution  $U(\tau, N_T)$  is

$$U(\tau, N_T) = \prod_l^{N_T} e^{-i\Delta\tau H_1/2} e^{-i\Delta\tau H_2} e^{-i\Delta\tau H_1/2}. \quad (\text{B3})$$

For Figure 12 (a) and (b), we employed the compressed circuit detailed in Fig.10 (b). The Trotterization using Eq. (B3) is used with  $N_T = 4$  and  $H_1 = -\frac{U}{2}(I + Z_1 Z_2)$  and  $H_2 = -t(X_1 + X_2)$ . These figures illustrate the robustness of our algorithm even in the presence of both of Trotterization errors and device noise. However, circuit compression may not always be feasible. To address this, we tested our algorithm with an uncompressed implementation of the Trotterization. This approach notably reduces  $\langle \Psi | \Psi \rangle$  due to the increased circuit depth compared to the compressed version.

To manage this depth, we employed QZMC with a reference state (Fig. 8). The reference state used was  $|\Psi_{\text{ref}}\rangle = [1/\sqrt{2} \ 0 \ 0 \ -1/\sqrt{2}]^T$ , representing the first excited state of the Hamiltonian. So, in Fig. 12 (c) and (d), we used  $N_\alpha = 4$ , with  $N_T = 1$ . We averaged two different Trotterization choices (one with  $H_2 = -\frac{U}{2}(I + Z_1 Z_2)$  and the other with  $H_2 = -t(X_1 + X_2)$ ) as this choice significantly influences computational results when Trotterization steps are small. We can see that, with the circuit Fig. 8 (d), QZMC gives accurate energy values, though it reduces  $\langle \Psi | \Psi \rangle$ . The circuits that we used for the QZMC with uncompressed Trotterization are depicted in Figure 13. Fig. 13 (a) represents the initialization circuit, while Fig. 13 (c) mimics the noise of the controlled-ZZ operation depicted in Figure 13 (b).

#### Appendix C: Details of noiseless simulator calculations

Here, we discuss more detailed information of the large size Hubbard models considered in the main text. The Hubbard

model is described by the Hamiltonian

$$H = - \sum_{\langle ij \rangle \sigma} t_{ij} c_{i\sigma}^\dagger c_{j\sigma} - \sum_i \mu (n_{i\uparrow} + n_{i\downarrow}) + \sum_i U n_{i\uparrow} n_{i\downarrow}. \quad (\text{C1})$$

The first two terms represent the kinetic energy and are denoted as  $H_t$ , while the last term represents electron-electron interaction and is referred to as  $H_U$ . First, we present the quantum circuit for the ground state of the Hubbard dimer in Figure. 14. Here, the angle  $\theta_d$  is given by

$$\theta_d = -2 \arctan \left( \frac{1}{2t} \left( \frac{U}{2} + \sqrt{\frac{U^2}{4} + 4t^2} \right) \right). \quad (\text{C2})$$

In the simulation, we used  $N_\nu$  and trotter steps  $N_T$  that varies with system size, and we fixed the number of shots  $N_s = 10000$ . Based on Eq. (A42), we determined  $N_\nu$  to be proportional to  $\|H'\|^2$ , which can be calculated as  $\|H'\| = t \times (\# \text{ of sites})$  for a chain and  $\|H'\| = 4t/\pi \times (\# \text{ of sites})$  for a ladder. And the proportionality constant is determined by testing  $6 \times 1$  system. The first order Trotterized time evolution  $U_1(\tau)$  of the Hubbard model with  $N_T$  trotter steps gives a Trotter error of [42]

$$\|e^{-iH\tau} - U_1(\tau)\| \leq \frac{\tau^2}{2N_T} \|[H_t, H_U]\|. \quad (\text{C3})$$

Then,

$$\|[H_t, H_U]\| \leq \sum_{\langle ij \rangle \sigma} t_{ij} U \| [c_{i\sigma}^\dagger c_{j\sigma}, \sum_i n_{i\uparrow} n_{i\downarrow}] \|. \quad (\text{C4})$$

Since all orbital indices are equivalent,  $\|[c_{i\sigma}^\dagger c_{j\sigma}, \sum_i n_{i\uparrow} n_{i\downarrow}]\|$  remains constant for any  $i$  and  $j$ . Consequently,  $\|[H_t, H_U]\| \leq CU(t_{\text{intra}}N_{\text{intra}} + t_{\text{inter}}N_{\text{inter}})$  for some constant  $C$ .  $N_{\text{intra}}$  denotes the number of intra-dimer hoppings and  $N_{\text{inter}}$  represents the number of inter-dimer hoppings. Based on this, we determined  $N_T$  as

$$N_T = \text{int} \left[ 75 \times \frac{\beta^2 U}{9 \cdot 5} \frac{(t_{\text{intra}}N_{\text{intra}} + t_{\text{inter}}N_{\text{inter}})}{8} \right] \quad (\text{C5})$$

with a minimum  $N_T = 20$ .

We depict  $\langle \Psi | \Psi \rangle$  for Hubbard models in Figure 15 (a)-(f). These figures demonstrate that increasing  $N_\alpha$  proportionally to the number of sites yields similar values of  $\langle \Psi | \Psi \rangle$  across various Hubbard models we studied. Fig. 15 (g) and (h) display spectral functions calculated with QZMC for 6-site Hubbard models.

- 
- [1] P. Benioff, The computer as a physical system: A microscopic quantum mechanical hamiltonian model of computers as represented by turing machines, *J. Stat. Phys.* **22**, 563 (1980).  
[2] R. P. Feynman, Simulating physics with computers, *Int. J. Theor. Phys.* **21** (1982).  
[3] M. A. Nielsen and I. L. Chuang, *Quantum computation and*

- quantum information* (Cambridge university press, 2010).  
[4] Y. Shen, D. Camps, A. Szasz, S. Darbha, K. Klymko, D. B. Williams-Young, N. M. Tubman, and R. V. Beeumen, Estimating eigenenergies from quantum dynamics: A unified noise-resilient measurement-driven approach, [arXiv:2306.01858](https://arxiv.org/abs/2306.01858) (2023).

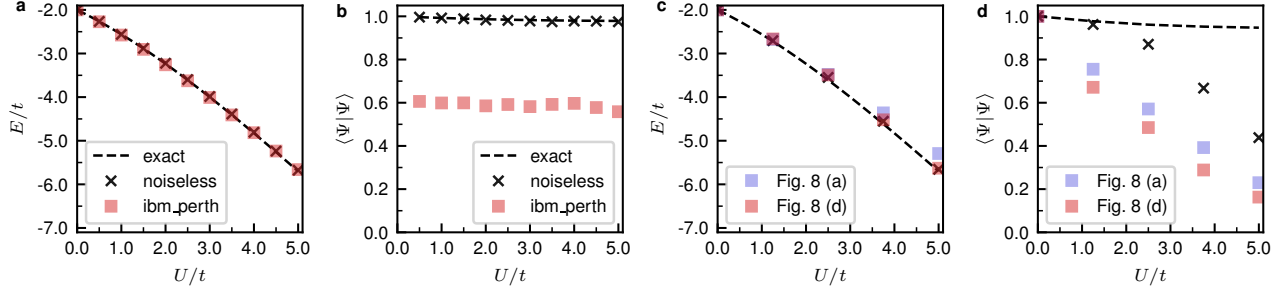


Figure 12. QZMC for the Hubbard dimer with the Trotterized time evolution. In (a) and (b), we used compressed circuit (Fig. 10 (b)), while the time evolution is computed with the trotter steps of 4. In (c) and (d), we used uncompressed Trotterized time evolutions. In (c) and (d), red square calculated from the circuit Fig. 8 (d), while blue ones are calculated with Fig. 8 (a). In this figure, squares are computed using *ibm\_perth*, while gray crosses are for the noiseless simulation and the dotted line represent exact results. In every calculations, we used  $\beta = 0.5$ ,  $N_\nu = 100$ .

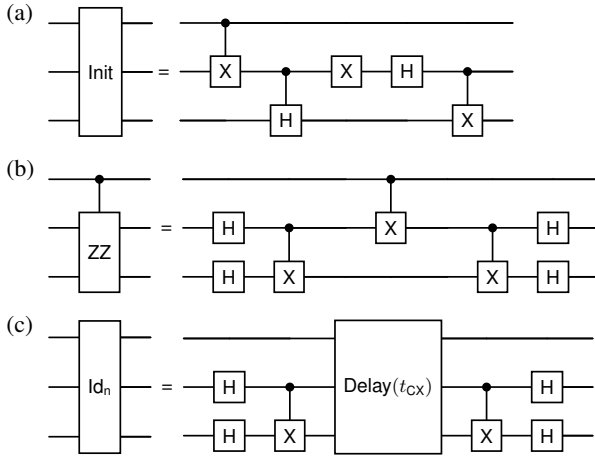


Figure 13. Quantum circuits for the Hubbard dimer. (a) is the initialization circuit for the ground state of the Hubbard dimer used in the QZMC with a reference state. The implementation of controlled-ZZ is drawn in (b). To mimic error induced by controlled-ZZ, we used the noisy identity circuit (c). In (c),  $t_{CX}$  represent the duration that CNOT operation the Delay( $t$ ) means the machine wait the duration of  $t$ .

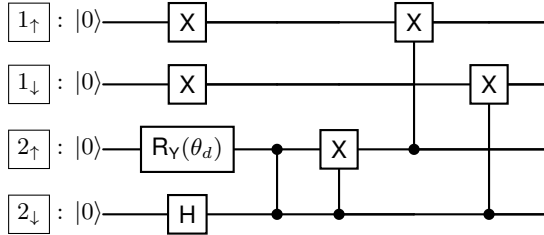


Figure 14. Quantum circuit for the ground state of the Hubbard dimer. The Quantum circuit that prepares the ground state of the Hubbard dimer is depicted. Here,  $\theta_d$  is defined in Eq. (C2).

- [5] A. Y. Kitaev, Quantum measurements and the abelian stabilizer problem, [arXiv:quant-ph/9511026](https://arxiv.org/abs/quant-ph/9511026) (1995).
- [6] D. S. Abrams and S. Lloyd, Quantum algorithm providing exponential speed increase for finding eigenvalues and eigenvectors, *Phys. Rev. Lett.* **83**, 5162 (1999).
- [7] P. W. Shor, Fault-tolerant quantum computation in *Proc. 37th Conference on Foundations of Computer Science* (IEEE, 1996), pp. 56-65.
- [8] D. Gottesman, Theory of fault-tolerant quantum computation, *Phys. Rev. A* **57**, 127 (1998).
- [9] J. Preskill, Quantum Computing in the NISQ era and beyond, *Quantum* **2**, 79 (2018).
- [10] A. Peruzzo, J. McClean, P. Shadbolt, M.-H. Yung, X.-Q. Zhou, P. J. Love, A. Aspuru-Guzik, and J. L. O'Brien, A variational eigenvalue solver on a photonic quantum processor, *Nat. Commun* **5**, 4213 (2014).
- [11] J. R. McClean, J. Romero, R. Babbush, and A. Aspuru-Guzik, The theory of variational hybrid quantum-classical algorithms, *New J. Phys.* **18**, 023023 (2016).
- [12] D. Bluvstein, S. J. Evered, A. A. Geim, S. H. Li, H. Zhou, T. Manovitz, S. Ebadi, M. Cain, M. Kalinowski, D. Hangleiter, *et al.*, Logical quantum processor based on reconfigurable atom arrays, *Nature* **626**, 58 (2024).
- [13] D. W. Berry, B. L. Higgins, S. D. Bartlett, M. W. Mitchell, G. J. Pryde, and H. M. Wiseman, How to perform the most accurate possible phase measurements, *Phys. Rev. A* **80**, 052114 (2009).
- [14] B. L. Higgins, D. W. Berry, S. D. Bartlett, H. M. Wiseman, and G. J. Pryde, Entanglement-free heisenberg-limited phase estimation, *Nature* **450**, 393 (2007).
- [15] B. Misra and E. G. Sudarshan, The zeno's paradox in quantum theory, *J. Math. Phys.* **18**, 756 (1977).
- [16] R. D. Somma, S. Boixo, H. Barnum, and E. Knill, Quantum simulations of classical annealing processes, *Phys. Rev. Lett.* **101**, 130504 (2008).
- [17] D. Poulin and P. Wocjan, Preparing ground states of quantum many-body systems on a quantum computer, *Phys. Rev. Lett.* **102**, 130503 (2009).
- [18] S. Boixo, E. Knill, R. D. Somma, Eigenpath traversal by phase randomization., *Quantum Inf. Comput.* **9**, 833 (2009).
- [19] H.-T. Chiang, G. Xu, and R. D. Somma, Improved bounds for eigenpath traversal, *Phys. Rev. A* **89**, 012314 (2014).
- [20] L. Lin and Y. Tong, Optimal polynomial based quantum eigenstate filtering with application to solving quantum linear systems, *Quantum* **4**, 361 (2020).

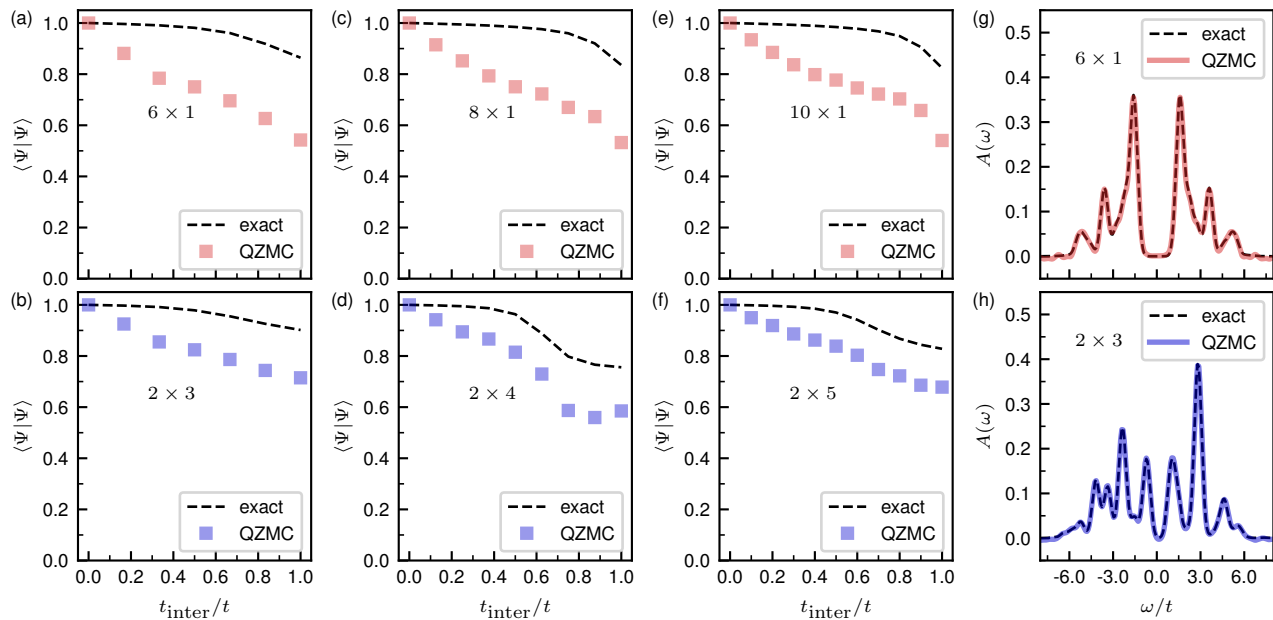


Figure 15. The half-filled Hubbard model in various sizes with QZMC. We plotted the  $\langle \Psi | \Psi \rangle$  for various sized Hubbard model in (a)-(f), and the spectral function for 6-site Hubbard models are plotted in (g) and (h).

- [21] J. H. van Vleck, Nonorthogonality and ferromagnetism, *Phys. Rev.* **49**, 232 (1936).
- [22] W. Kohn, Nobel lecture: Electronic structure of matter—wave functions and density functionals, *Rev. Mod. Phys.* **71**, 1253 (1999).
- [23] P. Zeng, J. Sun, and X. Yuan, Universal quantum algorithmic cooling on a quantum computer, [arXiv:2109.15304](https://arxiv.org/abs/2109.15304) (2021).
- [24] M. Huo and Y. Li, Error-resilient Monte Carlo quantum simulation of imaginary time, *Quantum* **7**, 916 (2023).
- [25] G. Wang, D. S. França, R. Zhang, S. Zhu, and P. D. Johnson, Quantum algorithm for ground state energy estimation using circuit depth with exponentially improved dependence on precision, *Quantum* **7**, 1167 (2023).
- [26] J. Sun, L. Vilchez-Estevéz, V. Vedral, A. T. Boothroyd, and M. Kim, Probing spectral features of quantum many-body systems with quantum simulators, [arXiv:2305.07649](https://arxiv.org/abs/2305.07649) (2023).
- [27] S. Lloyd, Universal quantum simulators, *Science* **273**, 1073 (1996).
- [28] C. Zalka, Simulating quantum systems on a quantum computer, *Proc. R. Soc. London, Ser. A* **454**, 313 (1998).
- [29] D. P. Kroese, T. Taimre, and Z. I. Botev, *Handbook of Monte Carlo Methods* (John Wiley & Sons, 2011).
- [30] M. T. Heath, *Scientific computing: an introductory survey, revised second edition* (SIAM, 2018).
- [31] L. D. Landau and E. M. Lifshitz, *Quantum mechanics: non-relativistic theory*, Vol. 3 (Elsevier, 2013).
- [32] V. Shende, S. Bullock, and I. Markov, Synthesis of quantum-logic circuits, *IEEE TCAD* **25**, 1000 (2006).
- [33] R. F. Stewart, Small gaussian expansions of slater-type orbitals, *J. Chem. Phys.* **52**, 431 (1970).
- [34] P. J. J. O'Malley, R. Babbush, I. D. Kivlichan, J. Romero, J. R. McClean, R. Barends *et al.*, Scalable quantum simulation of molecular energies, *Phys. Rev. X* **6**, 031007 (2016).
- [35] M. Motta, C. Sun, A. T. Tan, M. J. O'Rourke, E. Ye, A. J. Minnich, F. G. Brandao, and G. K.-L. Chan, Determining eigenstates and thermal states on a quantum computer using quantum imaginary time evolution, *Nat. Phys.* **16**, 205 (2020).
- [36] J. T. Seeley, M. J. Richard, and P. J. Love, The bravyi-kitaev transformation for quantum computation of electronic structure, *J. Chem. Phys.* **137** (2012).
- [37] M. Steudtner and S. Wehner, Fermion-to-qubit mappings with varying resource requirements for quantum simulation, *New J. Phys.* **20**, 063010 (2018).
- [38] J. Hubbard and B. H. Flowers, Electron correlations in narrow energy bands, *Proc. R. Soc. London, Ser. A* **276**, 238 (1963).
- [39] J. W. Negele and H. Orland, *Quantum many-particle systems*, Advanced book classics (Westview, Boulder, CO, 1988) addison-Wesley edition.
- [40] <https://quantumai.google/qsim>.
- [41] H. F. Trotter, On the product of semi-groups of operators, *Proc. Am. Math. Soc.* **10**, 545 (1959).
- [42] D. Layden, First-order trotter error from a second-order perspective, *Phys. Rev. Lett.* **128**, 210501 (2022).
- [43] <https://www.ibm.com/quantum/qiskit>.
- [44] J. Tilly, H. Chen, S. Cao, D. Picozzi, K. Setia, Y. Li, E. Grant, L. Wossnig, I. Rungger, G. H. Booth, and J. Tennyson, The variational quantum eigensolver: A review of methods and best practices, *Phys. Rep.* **986**, 1 (2022).
- [45] J. Watrous, Quantum computational complexity, [arXiv:0804.3401](https://arxiv.org/abs/0804.3401) (2008).
- [46] Z. Ding and L. Lin, Even shorter quantum circuit for phase estimation on early fault-tolerant quantum computers with applications to ground-state energy estimation, *PRX Quantum* **4**, 020331 (2023).
- [47] L. Lin and Y. Tong, Heisenberg-limited ground-state energy estimation for early fault-tolerant quantum computers, *PRX Quantum* **3**, 010318 (2022).
- [48] R. D. Somma, Quantum eigenvalue estimation via time series analysis, *New J. Phys.* **21**, 123025 (2019).
- [49] H. Ni, H. Li, and L. Ying, On low-depth algorithms for quantum

- phase estimation, [Quantum 7, 1165 \(2023\)](#).
- [50] V. V. Shende, I. L. Markov, and S. S. Bullock, Minimal universal two-qubit controlled-not-based circuits, [Phys. Rev. A 69, 062321 \(2004\)](#).
- [51] A. W. Cross, L. S. Bishop, S. Sheldon, P. D. Nation, and J. M. Gambetta, Validating quantum computers using randomized model circuits, [Phys. Rev. A 100, 032328 \(2019\)](#).